remote sensing

MDPI

Article

Volumetric Change Detection with SfM Photogrammetry from Rapid-Response Aerial Imagery After Hurricane Helene

Corey T. White [1,2,*], Pratikshya Regmi [1], William Reckling [1,3,4] and Helena Mitasova [1,3]

[1] Center for Geospatial Analytics, North Carolina State University, Raleigh, NC 27695, USA; pregmi3@ncsu.edu (P.R.)
[2] OpenPlains Inc., Durham, NC 27713, USA
[3] Department of Marine, Earth, and Atmospheric Sciences, North Carolina State University, Raleigh, NC 27695, USA
[4] Engineer Research and Development Center (ERDC), U.S. Army Corps of Engineers, Alexandria, VA 22315, USA
* Correspondence: ctwhite@ncsu.edu

Highlights

What are the main findings?

- After road-based co-registration and before bias correction, bare-earth models from uncontrolled Civil Air Patrol imagery match independent post-event LiDAR on the stable-terrain mask to a vertical error (NMAD) of 0.68 m in the open Swannanoa Valley and 0.82 m in the forested Hickory Nut Gorge, and 0.48 and 0.52 m on the mask cells where the raw difference is defined.
- In the Swannanoa Valley the workflow measured 125,000 m^3 of erosion and 123,000 m^3 of deposition between the 2017 LiDAR and the 2024 CAP sortie, about 13% of it dating to the sortie. In Hickory Nut Gorge at Chimney Rock it measured 76,000 m^3 of erosion and 84,000 m^3 of positive change, just under half of that change dating to the sortie.

What are the implications of the main findings?

- Calibrating the Level of Detection on the heavy-tailed residuals and letting it vary in space both matter: the valley DSM limit is 7.9 m at median window dispersion, against 2.09 m for a Gaussian limit from road control, and ranges from 6.5 m to 192 m at structure edges.
- Both flights support volumetric change only on open ground, where the testable bare-earth domain covers 5.6% of the valley hull and 1.1% of the forested gorge hull.

Abstract

Civil Air Patrol (CAP) imagery, often the first post-disaster observation, is designed for 2D interpretation rather than multi-temporal volumetric measurement. We build post-storm digital surface and terrain models from uncontrolled CAP imagery with structure-from-motion in western North Carolina's open Swannanoa Valley and forested Hickory Nut Gorge. Surfaces are co-registered to pre-event LiDAR using roads as pseudo ground control, corrected for terrain-correlated bias, and thresholded with a spatially variable, calibrated Level of Detection. Before bias correction, bare-earth surfaces match withheld post-event LiDAR on stable terrain to 0.68 and 0.82 m normalized median absolute deviation. Volumes are 2017-to-2024 change, lower bounds in coverage, and conditional on the bias model, residual screen, and detection window. Corrected valley surfaces record 125,000 m^3 of erosion and 123,000 m^3 of deposition, and a sampled image check dates about 13% of that change to the sortie. Under the same limit, the uncorrected surface reports five times the deposition, and the alternative bias model gives gross terms 3.6 to 4.2 times larger. The gorge

Check for updates

Academic Editor: Wen Liu

Received: 21 August 2026
Revised: 23 October 2026
Accepted: 26 October 2026
Published: 1 November 2026

Copyright: © 2026 by the authors. Licensee MDPI, Basel, Switzerland. This article is an open access article distributed under the terms and conditions of the Creative Commons Attribution (CC BY) license.

at Chimney Rock recorded 76,000 m^3 of erosion and 84,000 m^3 of positive change, just under half dating to the sortie, including land deposition partly cleared before the post-event LiDAR flew. CAP-derived surfaces can capture transient storage that later surveys cannot.

Keywords: structure-from-motion; photogrammetry; DEM of difference; change detection; landslide; disaster response; LiDAR; Hurricane Helene; GRASS

1. Introduction

Post-storm aerial imagery is often the only information emergency managers have until communication networks are reestablished [1,2]. Visual interpretation, spectral indices such as the Normalized Difference Vegetation Index (NDVI), and machine learning locate damaged roads and buildings, landslides, and floods in 2D imagery [3–6] for resource allocation, route planning, and damage estimation [7]. Volumetric 3D change detection is rare in operational response, and post-storm LiDAR is seldom available in the immediate aftermath [8].

The Helene response illustrates the limitation. The U.S. Geological Survey (USGS) mapped 2217 landslides across a ~250 km swath of the Blue Ridge escarpment from 2D products such as NDVI change maps and oblique aerial photos, which located landslides but could not quantify the volumes that debris management, infrastructure assessment, and sediment budgets require [9]. Debris volumes were estimated from aerial photography during the response [10], with early products from the workflow presented here shared in that effort [11], but a systematic evaluation of such image-derived volumetrics against independent data has been missing.

The Civil Air Patrol (CAP), a U.S. Air Force Auxiliary unit, flies rapid-response aerial imagery after disasters, and although the flights are suitable for photogrammetry, 3D products are a byproduct rather than the end result [12]. Three existing 3D-capable sources frame the gap. NOAA National Geodetic Survey (NGS) crewed-aircraft emergency response imagery follows U.S. landfalling hurricanes within days and reached the two corridors studied here two days after the CAP sorties at 15–30 cm mosaic resolution [13,14]. Structure-from-motion (SfM) reconstruction of such frames has mapped coastal change within about 48 h at 0.20–0.25 m vertical RMS against LiDAR [15], and crewed-aircraft imagery served 3D debris assessment after Helene itself [16]. Satellite stereo digital surface models (DSMs) reach sub-meter accuracy after stable-terrain co-registration but at 2–4 m native posting and under tasking and weather constraints [17–20]. Archival photogrammetry reconstructs topography from uncontrolled historical frames by co-registering to a modern reference terrain [21–25]. None of these provides, for inland flood response, opportunistic nadir imagery from an already-flying emergency program, vertical control from nothing but pre-event road surfaces, and an independent evaluation against post-event LiDAR: an accuracy assessment of the surfaces on stable terrain, and a consistency evaluation and false-positive bound for the change products.

We present that combination as a workflow, applied to two sites in western NC mapped by CAP days after Hurricane Helene. The primary novelty of this study is quantitative volumetric change assessment from uncontrolled CAP imagery, delivered with a stable-terrain accuracy assessment of the surfaces and a consistency evaluation of the change against independent post-event LiDAR. Three elements make it possible: (1) vertical control recovered from pre-event road surfaces as pseudo ground control, (2) an empirical correction for the terrain-correlated elevation bias that uncontrolled SfM blocks carry, and (3) an empirically calibrated, spatially variable Level of Detection that states where change is testable. Two contrasting environments, an open valley and a forested gorge, serve to test the workflow.

2. Materials and Methods

The change-detection workflow downstream of the photogrammetry is implemented as r.dem [26], an open-source addon toolset for GRASS [27] developed for this work. The tools are mapped to their steps and parameters in Supplementary Table S5, and shown together in Supplementary Figure S9.

2.1. Study Areas

Hurricane Helene made landfall as a category 4 hurricane on 26 September 2024, and over the following three days caused inland flooding with more than 250 deaths and damages estimated at USD 78.7 billion [28]. The CAP provided the first post-event images, and we selected the Swannanoa Valley and the Hickory Nut Gorge (Figure 1) for the severity of the reported damage.

2.1.1. Swannanoa Valley

The Swannanoa Valley, in Buncombe County east of Asheville, drains west along the Swannanoa River to the French Broad River. Community Collaborative Rain, Hail and Snow Network (CoCoRaHS) stations NC-BC-115, southeast of Black Mountain, and NC-BC-25, near Swannanoa, recorded 53.5 and 51.4 cm of rainfall during Helene, and the USGS gauge at Biltmore (03451000), downstream of the study reach, reached a gauge height of 8.33 m above the gauge datum on 27 September 2024, above the 6.31 m peak of July 1916 and the 7.92 m historic estimate for an April 1791 flood [29]. CAP Flight A0046B photographed the valley on 3 October 2024, 6 days after the 27 September flooding of western North Carolina [30].

2.1.2. Hickory Nut Gorge

The Hickory Nut Gorge runs from Bearwallow and Chimney Rock to Lake Lure in Rutherford County, along NC State Highway 9 and the Rocky Broad River. The Lake Lure Dam watershed received approximately 57.2 cm of rainfall from September 24 through 28 [31], and the Rocky Broad River crested several meters above any previous record. The gorge's steep SE-facing slopes lay in the zone of highest landslide susceptibility during Helene [9]. Landslides and debris flows destroyed most of Chimney Rock's buildings, homes, and businesses [28], and an estimated 1 million cubic yards ($\sim 7.6 \times 10^5$ m^3) of debris was later removed from Lake Lure [32]. CAP Flight A0069AR photographed the gorge on 5 October 2024, 8 days after that flooding [30].

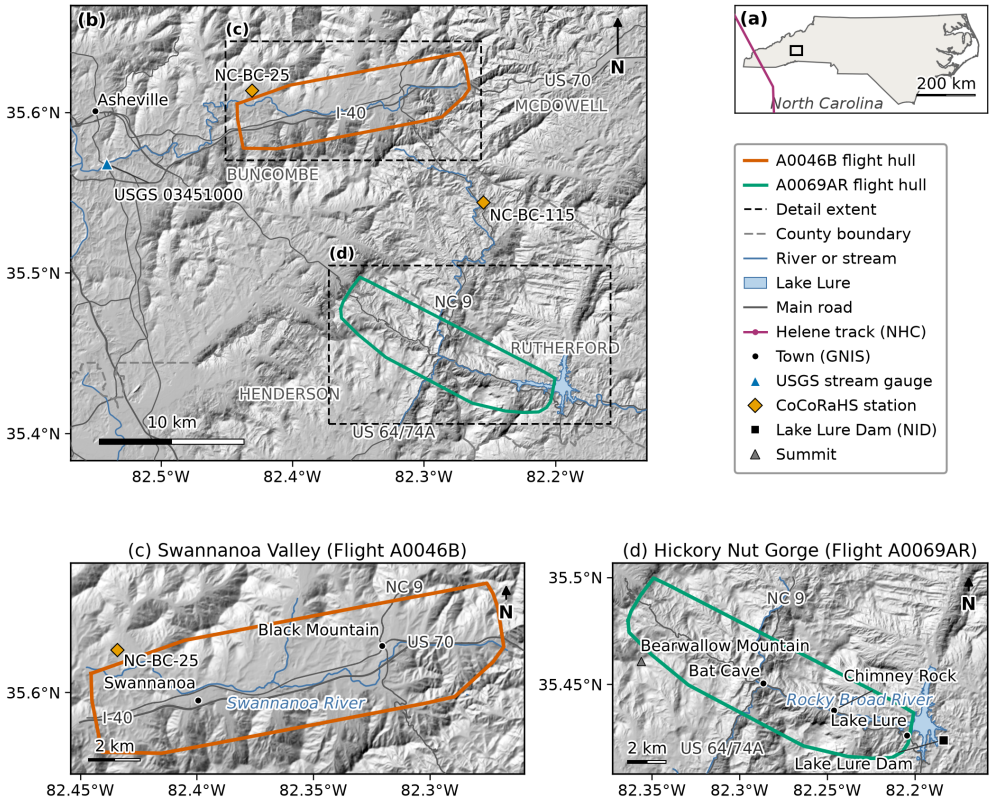


Figure 1. Study areas in western North Carolina. (**a**) North Carolina with the Hurricane Helene best track (NHC ATCF AL092024 [28,33]) and the extent of panel (**b**); (**b**) regional overview with the two flight hulls and the detail panel extents; (**c**) the Swannanoa Valley (Flight A0046B, Buncombe County); (**d**) the Hickory Nut Gorge (Flight A0069AR, Rutherford County) from Bat Cave and Chimney Rock along the Rocky Broad River to Lake Lure.

2.2. Data

Of the data sources in Table 1 (raw CAP frames in Supplementary Figure S1), the CAP photos [30] yield the post-storm SfM surfaces. The 2017 USGS original product resolution (OPR) digital elevation model (DEM), a bare-earth digital terrain model (DTM) [34], and a first-return DSM binned from the same point cloud [35,36] are the pre-storm references, and the post-event LiDAR [37] is reserved for validation. All analysis ran in NAD83(2011)/UTM 17N with NAVD88 heights in meters (EPSG:6346+5703) in GRASS on a 1 m grid.

Table 1. Data sources used in the analysis.

Name	Year	Type	EPSG	Source
CAP Imagery	2024	Imagery	4326	[30]
NC Orthos	2019	Imagery	6543	[38]
NC Orthos (pre-event)	2020–2023	Imagery	6346	[39]
NC Orthos (post-Helene)	2025	Imagery	6346	[40]
NC LiDAR (pre-event)	2017	DSM/DTM	6543 *	[35,36]
NC LiDAR (post-event)	2025	DSM/DTM	6543 *	[37]
USGS OPR DEM (3.125 ft)	2017	DTM	6543 *	[34]
Roads	2026	Vector	6543	[41]
NHD flowlines	2026	Vector	4269	[42]
Parcels	2025	Vector	6543	[43]

* Compound EPSG:6543+6360 (NC State Plane, NAVD88 heights in US survey feet); the 2017 LiDAR and OPR DEM realize NAVD88 through GEOID12B and the post-event LiDAR through GEOID18. Year is the acquisition year for imagery and LiDAR and the snapshot year for the quarterly road and hydrography services.

The photos (mission 24-1-5849) were flown on a single grid with Canon EOS 5DS R cameras (Canon Inc., Tokyo, Japan), georeferenced by GPS (WGS84, EPSG:4326) [12], at CAP's nominal overlap setting of 75% forward and 60% side [44], a planning value rather than one measured for these sorties. Near-vertical (nadir) photos were captured by adjusting the aircraft's roll angle to bring the camera pitch angle ϕ to near 90° [12].

The OPR DEM is the vendor's hydro-flattened bare-earth DEM of the NC Phase 5 LiDAR, delivered as 3.125 ft tiles (work units NC_Phase5_Buncombe_2017 for A0046B and NC_Phase5_Rutherford_2017 for A0069AR). That LiDAR was collected leaf-off between 10 February and 10 April 2017 at QL1 (USGS Quality Level 1) [35,36], with a published non-vegetated vertical accuracy (NVA) of 15.7 cm at 95% confidence and a vegetated vertical accuracy (VVA) of 22.8 cm at the 95th percentile [45,46]. Its tiles were resampled bilinearly to the 1 m grid and their NAVD88 heights converted from US survey feet to meters (factor 1200/3937), with the vertical datum handled explicitly (Supplementary Methods SM1).

Post-event LiDAR (25 January to 15 February 2025, NC Collaboratory/NC Emergency Management leaf-off campaign, specified as classified QL1 [47]) was not used in co-registration or bias correction (Sections 2.6 and 3.3), and because it postdates the storm, its difference against the co-registered SfM isolates SfM error plus intervening recovery change rather than storm change. No vertical accuracy report for this campaign had been published by October 2026. QL1 requires a non-vegetated $RMSE_z$ of at most 0.10 m (0.196 m NVA at 95% confidence) [48], and with the 15.7 cm NVA of the 2017 data ($RMSE_z$ about 0.08 m) the combined error of the two surveys on unchanged open ground is at most about 0.13 m RMSE. It was binned to 1 m DSM (maximum Z) and DTM (minimum Z of classes 2 and 11) surfaces on the same grid. Orthometric heights follow $H = h - N$, the ellipsoidal height h reduced by the geoid undulation N, so differencing NAVD88 realizations built on GEOID12B [49] (used for the 2017 data) and GEOID18 [50] (used for the post-event data), both taken from the PROJ-data distribution [51], carries the mapped separation of the two hybrid geoid models as a systematic term. That separation is smooth and bounded by 1.7 cm over both study areas (Supplementary Figure S10 and Note S7); it was bounded, not applied as a correction. The stable-terrain median inter-epoch difference (post-event LiDAR minus 2017 LiDAR on the stable mask of Section 2.6) is below 0.01 m for A0046B and −0.10 m for A0069AR, within that combined error, and it is left in the validation statistics (Section 3.3). The SfM block itself carries no realized vertical datum: the EXIF altitude is flagged as a height above mean sea level (Table A1), and Metashape loaded the camera positions as WGS 84 (EPSG:4326) and exported the products in EPSG:6346 with those heights. The shifts of Section 2.5 show the EXIF altitudes are geoid-referenced: the GEOID18 undulation is −30.0 and −31.1 m at the two study areas, so ellipsoidal altitudes would place the SfM surfaces about 30 m below the LiDAR, whereas the road-median shifts put them 3.71 to 5.37 m above it. The road-PGCP median shift of Section 2.5 is therefore the block's only realization of NAVD88, and the raw shifts it removes (5.37 and 5.03 m for A0046B, 3.71 m for A0069AR) combine that unresolved datum with the aircraft GPS bias and are not accuracy figures.

2.3. SfM Photogrammetric Processing

CAP imagery was processed in Agisoft Metashape Professional v2.2 [52] (versions per flight in Supplementary Methods SM1) and GRASS 8.5 [27]. Camera positions came from the EXIF GPS tags, no ground control was deployed, and the archive holds near-vertical imagery only. Without oblique views or ground control the block geometry is weaker than a controlled survey [53,54], leaving a terrain-correlated elevation bias that Section 2.6 characterizes and corrects empirically.

After images with a quality score below 0.7 were disabled, self-calibration and bundle adjustment ran at original resolution [55,56] with stationary tie points excluded [57], the

sparse cloud was filtered by reconstruction uncertainty, projection accuracy, and reprojection error with camera re-optimization between passes [58], and the distortion model ($f, c_x, c_y, b_1, b_2, k_1$–$k_3, p_1, p_2$) was fit with adaptive fitting disabled [55,59]. The dense cloud, built from high-quality depth maps, cleaned of single-depth-map points for A0046B (report point confidence 2 to 15; the A0069AR cloud retains them, confidence 1 to 21), and decimated to three times a ground sampling distance (GSD) the script estimated from focal length, pixel pitch, and flying height (point spacing 0.44 m for A0046B and 0.74 m for A0069AR), was ground-classified by the batch script with progressive TIN densification tuned for steep terrain. The script's multi-class step assigned no classes, so the final classes (vegetation, building, road surface, and others) were assigned interactively in Metashape at a classifier confidence of 0.2 (A0046B) and 0.01 (A0069AR), with misclassified points on A0069AR corrected by hand, among them buildings labeled in steep forest. The settings and extent of the interactive step were not logged. It left the A0069AR ground class within a net 2302 of the script's 20.87 million points but reassigned most A0046B ground points (28.6 of 121.8 million remain ground), so both DTMs, built from the ground and road classes, are evaluated as built against the post-event LiDAR on stable terrain (Section 3.3), and the interactive step cannot be rerun exactly. From the classified point cloud onward, every step for both flights (surface building, co-registration, bias correction, detection limits, volumes, and validation) runs from the per-flight configuration file. All parameters are listed in Supplementary Methods SM1, and the stale fields of the Supplementary flight reports are reconciled with the values applied in the flight-report notes of the Supplementary Materials.

The maximum-elevation DSM and the ground- and road-return DTM were built from the classified cloud with the DTM interpolation matched to each landscape. In the Swannanoa Valley (A0046B), ground returns were interpolated with regularized spline with tension (RST) [60–62], with tension and smoothing selected by leave-one-out cross-validation. In the forested gorge (A0069AR), ground returns under intact canopy were too sparse to constrain an interpolated surface, so the DTM was binned as the minimum ground return per cell, and gaps were interpolated (r.resamp.bspline, bicubic, default settings) only within the Stage 1 screening zones (Section 2.7) and the co-registration road corridors, with the 2017 LiDAR DTM substituted beyond a 30 m ring. The filled surface serves co-registration and display only: interpolated cells carry no ground returns and fail the point-density rule of Section 2.4, and every one of the 1.32 million valid gorge DoD cells holds at least one ground return, so no interpolated cell enters a volume.

The two flights differ in analyst, workstation, Metashape version, dense-cloud confidence filtering, decimation spacing, point classifier settings and manual class edits, DTM interpolation, bias model, and shift strategy, confounds that the two-flight comparison does not isolate. Valley-versus-gorge contrasts in this paper therefore describe these two flights as processed, not terrain alone.

Block-strength diagnostics from the Metashape processing reports are given in Supplementary Table S14. The native image GSD is ≈8 cm (orthomosaics at 7.95 and 8.34 cm/pixel). The ground resolution the reports list, 44 and 74 cm/pixel, is the DEM resolution Metashape derives from the decimated cloud's point density, $1/\sqrt{5.16\ \mathrm{m}^{-2}} = 0.44$ m and $1/\sqrt{1.84\ \mathrm{m}^{-2}} = 0.74$ m, so it reflects decimation and coverage, not image texture. The camera-location residuals against the onboard GPS show no gross vertical mis-scaling (Z residual ~0.9 m; an internal-consistency check that cannot exclude a focal-length error, Section 2.6) while the horizontal residuals are large and anisotropic (X 17.0 and 13.9 m, Y 3.7 and 7.0 m, structured along flight lines in the reports), which the PGCP shift does not correct and the horizontal-offset checks of Section 2.5 bound (Supplementary Table S14).

2.4. Dual-Surface Change-Detection Framework

For each surface, after the co-registration of Section 2.5, the DEM of Difference (DoD) $\mathrm{DoD} = \mathrm{SfM}_{\mathrm{coreg}} - \mathrm{LiDAR}$ is computed against the matching LiDAR product and thresholded against the Level of Detection (LoD, Section 2.8; Figure 2). DSM change is limited to cells with zero vegetation-classified SfM returns, so canopy-height differences are not read as geomorphic change while destroyed structures and landslide scars, which read as bare ground, survive. The bare-earth DoD is further restricted to cells with a ground-return density of at least 0.5 points/m^2 and a raw SfM DSM − DTM separation below 3 m, a canopy check that removes vegetation and structures the classifier missed. The DoD domain carries no separate water rule: cells inside the 15 m hydrography buffer of Section 2.6 enter where the SfM surface has ground returns at that density (38% of the buffered channel cells for A0046B, 1.3% for A0069AR), and the profile figures label buffer cells without a valid DoD as water-masked; post-storm channel positions outside the pre-storm buffer, such as the avulsed reach below Chimney Rock, are treated as open ground, where the SfM surface may record water or a refraction-shallowed bed against 2017 ground and so understates erosion. The buffer follows the flowlines only, so hydro-flattened 2017 surfaces beyond it, such as the open water of Lake Lure and wider river reaches, are not masked; it holds 2452 of the 162,288 significant A0046B cells (1800 and 2100 m^3 of deposition and erosion) and 1229 of the 47,178 gorge cells (3300 and 700 m^3), and the hydro-flattened 2017 Lake Lure surface carries 3822 significant gorge cells, 3692 of them outside the buffer (Section 3.2.4). The valley cells on hydro-flattened surfaces outside the buffer were not counted, and the in-buffer figures give their scale. Stable-mask cells are not excluded from the tally (Section 3.1.5). In the forested A0069AR footprint both surfaces are restricted to open ground (pre-event canopy height below 2 m) and share a single vertical shift (Section 3.2.2). The DTM isolates sediment erosion and deposition, and the DSM adds the loss or gain of buildings, debris, and vegetation.

2.5. Co-Registration

The CAP sorties, flown for damage assessment, collected no ground control. We sampled pseudo ground control points (PGCPs) from buffered state-highway road centerlines, where the post-event SfM and pre-event LiDAR surfaces image the same unchanged pavement, and removed their median residual as a single vertical shift.

$$\mathrm{SfM}_{\mathrm{coreg}}(x,y) = \mathrm{SfM}(x,y) - \tilde{b}, \qquad \tilde{b} = \mathrm{median}\Big[\mathrm{SfM}(x,y) - \mathrm{LiDAR}(x,y)\Big]_{\mathrm{PGCP}}. \quad (1)$$

The centerlines are a 2026 Q1 snapshot of the NCDOT quarterly state-maintained roads service [41]. No road was excluded for resurfacing, reconstruction, or burial, since no record of such work was used. The median tolerates a minority of altered cells, and its uncertainty is reported in two parts (Supplementary Note S13 and Table S17). Sampling uncertainty, for the roads as selected, comes from a block bootstrap with blocks at least as wide as the range of a robust semivariogram of the road residuals [63,64]: 0.12 m for the A0046B shift and 0.16 m for the applied A0069AR shift. Road-selection uncertainty comes from a two-stage bootstrap that resamples NCDOT routes and then 250 m segments within them [65]: 0.10 m over 171 routes and 0.14 m over 51 routes, and dropping any one route moves the valley bare-earth shift or the shared gorge shift by at most 0.09 m. Outlying segments, whose median departs from the median of all segment medians by more than three NMAD of the segment medians (1.9 to 3.2 m, a threshold that catches rebuilt or buried road but not resurfacing), number 85 of 1196 in the valley and 63 of 372 in the gorge, and removing them moves the shift by −0.05 and +0.15 m. Because the elevation-only bias model carries a free intercept and the A0046B spline, fit to the same post-shift residuals, absorbs a uniform offset, a residual shift error changes no reported volume beyond its effect

on the centering of the residual screen (recentering it by twice the road-selection standard error moves the gross terms by at most 3.1% in the valley and 1.7% in the gorge), and the vertical datum of every volume is the debiased stable-mask mean rather than the road shift.

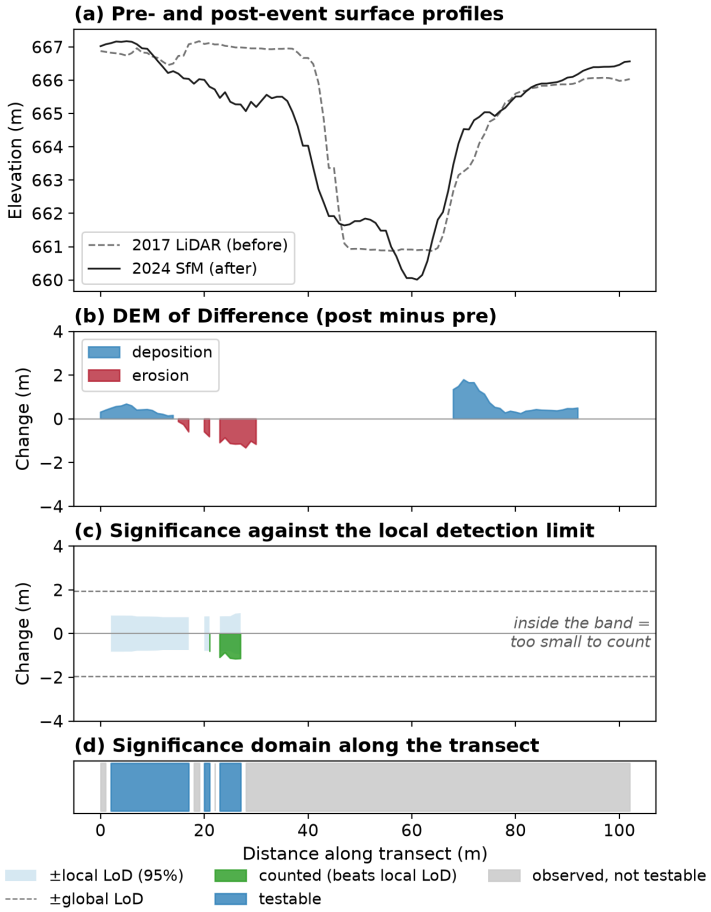


Figure 2. Change-detection test on the riverbank transect A–B (Flight A0046B; Section 3.1.3), drawn here in simplified form to define the test: (**a**) the 2017 LiDAR and 2024 SfM surfaces; (**b**) the bias-corrected DoD, blank where the bias field is undefined; (**c**) the significance test against the spatially variable local LoD band and the uniform global limit; (**d**) the reach where the local limit is defined, against observed but untestable cells. Change inside the band or outside the tested reach is not counted, so reported volumes are lower bounds.

The Nuth and Kääb cosine fit [66] and iterative closest point seeded with the road PGCPs (r.dem.icp) [67] were tested and not adopted, because the dominant error is elevation-dependent (Section 2.6) and no rigid transform represents it. For A0046B the Nuth and Kääb fit and phase cross-correlation [68] put the residual horizontal offset at 0.32 to 0.47 m, and the planimetric scale errors of the two blocks imply at most 0.16 and 0.38 m at the footprint edge; propagated at 0.40 m on both flights as an apparent vertical error $\delta \tan \theta$ (offset δ, local slope θ), it exceeds the per-cell detection limit on at most 0.03% of tested cells (Supplementary Note S4 and Table S8).

2.6. Elevation-Dependent Bias Correction

A uniform shift leaves an elevation-dependent error that grows with height above the valley-floor road control. Regressed on distance from the camera-block center, the pre-correction stable residual shows no radially symmetric doming about the block centroid on either flight ($R^2 < 0.001$) [69]; both camera blocks are elongated along their valleys, so this test cannot detect doming across the block axis, which would also appear as an

elevation dependence. For A0046B, height below the nearest camera station, the covariate a focal-length error scales with, fits the residual worse than elevation (R^2 0.010 against 0.023) and implies a scale error of 0.002 to 0.004, about 30 to 60 times the formal focal-length standard error of the bundle (6.7×10^{-5} of f, Supplementary Table S14); that standard error is a precision under the default camera-position weights rather than an accuracy bound, so the diagnostics do not support lens scale as the mechanism without excluding it. The elevation slope keeps its sign across an east/west split of each block (+0.44 and +0.32 m per 100 m for the A0046B halves), but the valley drains west, so the split does not test a roll about the valley axis, and neither a datum tilt from the valley-floor control geometry nor cross-axis doming is excluded. Elevation is therefore retained as the predictor, and the error is corrected empirically with its origin unresolved (Supplementary Note S5).

The bias is fit on a stable-terrain mask defined by four rules: (1) slope between 5 and 50° on the reference DTM; (2) canopy-free by the SfM point-cloud mask, with zero vegetation-classified returns (the bare-earth surfaces are built from ground- and road-classified points alone, and the SfM classifier carries no water class); (3) outside NHD flowlines (line features only, no waterbody polygons) buffered by 15 m, with flat wet sediment beyond the buffer removed by the 5° slope floor; and (4) a residual screen $|\mathrm{SfM} - \mathrm{LiDAR}| < 5$ m on the co-registered difference, symmetric about zero. Supplementary Table S9 varies the tolerance from 3 to 10 m and removes the screen entirely, with the bias fit and the windowed dispersion held at their canonical values, so the sweep isolates the screen's effect on the retained population and the coverage multiplier (and on the in-sample floor for A0069AR; the A0046B floor is held at the blocked cross-validation value, which was not recomputed per screen). Removing the screen changes the robust dispersion by under 0.01 m on nearly the same population (NMAD 0.20 m with and without it for A0046B, 0.76 against 0.75 m for A0069AR), with the heavy tail appearing only in the root mean square error (RMSE; 0.71 against 0.44 m and 1.40 against 1.04 m); with the fit held fixed, widening it to 10 m moves the gross volume terms by less than 4% on both flights and removing it by at most 4.2%, and tightening it to 3 m is the anti-conservative direction, raising the gorge positive term by 21% and the valley gross terms by 10 to 11%. Supplementary Table S16 reruns the whole chain on each screened mask, refitting the bias and rebuilding the local detection limit (Supplementary Note S12). The gorge regression barely moves (intercept within 0.03 m and slope within 0.004 m per 100 m of the adopted fit), and under the adopted limit its gross terms stay within 1.4% for tolerances of 3 to 10 m. Through the rebuilt limit they move by −20 to +15% over the same tolerances (+18% erosion without a screen). At 3 m the movement comes from the rebuilt limit inside the published tested domain, and at 7.5 and 10 m mostly from its edge, where the domain gains cells of which 2400 to 2700 are significant, carrying 12,600 to 13,900 m^3 of erosion. The valley spline is the sensitive fit. Under the adopted limit the refit alone moves the valley gross terms by −8 to +20%, against ±2.4% from resampling its 50,000 fit points with other seeds, and with the limit rebuilt on each mask they move by −4 to +11%. Its mean field changes most above 773 m (up to +0.25 m, against at most +0.06 m from resampling), but under 5% of the valley gross terms lie there, so the volumes move with smaller, spatially varying changes across the valley floor. Without any screen the spline absorbs real change at high elevation (mean field +1.08 m in the top decile) and valley erosion rises by 77%, the case the screen exists to prevent. The screen is not an outlier filter at high elevation, and at the adopted tolerance it removes 39% (A0046B) and 93% (A0069AR) of the candidate cells of the hull-wide masks: on A0046B the retained fraction falls from 0.85 in the lowest elevation decile to 0.15 in the highest, because the SfM error grows with height and canopy-edge cells increasingly trip the threshold, so above the valley floor the screen defines the fitting population (Supplementary Note S5). The elevation trend is weak but resolved. Least squares on a 300,000-cell random sample of

the whole stable mask (SfM DTM minus 2017 DTM, including mask cells where the DoD is undefined) gives +0.32 m per 100 m for A0046B and +0.08 m per 100 m for A0069AR, with bootstrap intervals excluding zero, and explains 2.3% of the residual variance (R^2 0.023, A0046B); on the 4.28 million A0046B stable cells where the raw DoD is defined the slope is +0.15 m per 100 m (Supplementary Figure S11, Supplementary Note S5). For A0046B the screened mask holds 8.08 million cells. The 4.28 million where the raw DoD is defined fit the bias models (50,000 sampled points for the spline, a 2 million-cell cap for the regression) and carry the blocked cross-validation (Figure 3); the 1.59 million where the bias-corrected DoD is defined carry the screen statistics of Supplementary Table S9; the 1.55 million inside the LoD domain calibrate k_{95} (Section 2.8); and the 1.01 million inside the post-event LiDAR footprint are the stable stratum of Table 3, of which 574,485 lie where the raw DoD is defined and 207,590 where the bias-corrected DoD is defined. For A0069AR the counts are 1.96 million (the hull-wide mask, which includes cells under canopy that the SfM point classifier labeled ground), 412,513 (the open-ground corridor cells where the raw DoD, and with it the regression correction, is defined, which fit the bias model, set the floor, and carry Supplementary Table S9), and 442,494 inside the post-event LiDAR footprint (the stable stratum of Table 3), of which 105,957 lie where the DoD is defined. The mechanism diagnostics use the 300,000-cell sample. On the 1.59 million cells where the bias-corrected DoD is defined the raw residual carries almost no elevation trend (−0.03 m per 100 m over a 35 m spread of elevation), so the trend is expressed in the stable cells above the footprint, and inside it the correction acts mainly through spatial structure (Section 3.1.5). The fitted field is checked against the post-event LiDAR over the elevation range of the check cells of Section 3.1.2.

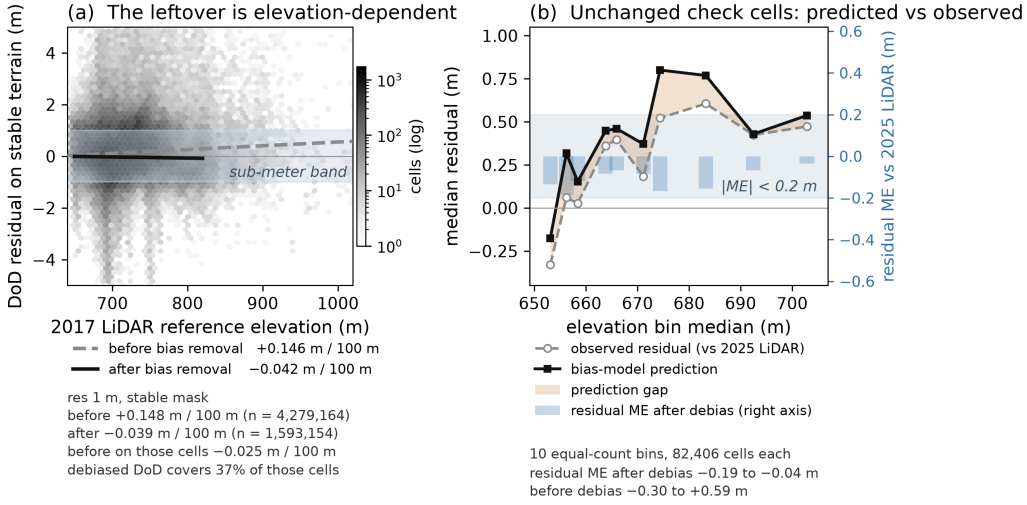


Figure 3. The elevation-dependent bias and its correction, Flight A0046B bare earth (the same panels appear in Supplementary Figure S11b,c). (**a**) Stable-terrain DoD residual against reference elevation, with least-squares trends before correction on the 4.28 million stable cells where the raw DoD is defined and after correction on the 1.59 million where the bias-corrected DoD is defined, drawn over that support; the legend slopes are fitted on the plotted 5 m subsample. On the same 1.59 million cells the raw trend is already −0.025 m per 100 m (note box), so the elevation trend lies in stable cells above the corrected footprint. (**b**) Elevation-binned check on independent check cells, open cells the post-event LiDAR shows unchanged (21% of them also bias-fit cells): observed median residual against the post-event LiDAR and the bias-model prediction in ten equal-count bins, with the mean error after correction on the right axis. The bin medians span 653 to 703 m, while the cells reach 890 m (Section 3.1.2).

The bias field is subtracted from the DoD before any thresholding (r.dem.bias; its effect on the valley tally is shown in Figure 4), as either a least-squares regression of the DoD on pre-event LiDAR elevation or a regularized spline with tension (v.surf.rst) fit to sampled stable residuals at 10 m under the valid-DoD mask and resampled bilinearly to 1 m, so it is defined only where the four surrounding 10 m cells fall inside the valid footprint; along the fragmented edges of the footprint this leaves 10.1 million of the 16.6 million valid A0046B cells without a correction, and they are reported as untestable (Supplementary Table S11; Supplementary Note S5). A spline fitted on stable cells can absorb real deposition. A four-predictor regression (slope, roughness, geomorphic diversity, elevation) was excluded before comparison because collinearity inverted the sign of its elevation term (Supplementary Note S5; listed in Supplementary Table S2 for reference only). The two candidates per flight are the elevation-only regression and the spline field, compared with three diagnostics, none of which decides alone (values in Supplementary Note S5). First, blocked cross-validation on stable cells (Section 2.8) favors the spline on both flights (held-out NMAD at 1 km blocks 0.46 against 0.72 m in the valley and 0.55 against 0.66 m in the gorge), but a field that absorbs deposits on a stable mask that carries them also scores well on held-out stable cells. Second, a zone contrast compares the structure the spline adds beyond the elevation-only model inside the Stage 1 screening zones of Section 2.7, which come from the independent 10 m screen, with its average on stable ground: the gorge spline adds +0.39 m inside the zones against +0.03 m on stable ground, and the valley spline −0.17 against −0.04 m overall but lowers its deposition zones by 0.80 m (0.84 m relative to stable ground). Third, under one limit calibrated on the regression's residuals for both flights, the spline has 2.6 times fewer significant cells than the regression in the valley and 4.4 times fewer in the gorge on the cells where both fields are defined, and 12 and 21 times fewer on each field's own support; the difference between the two counts is the spline's support rule, which leaves it undefined on 61% of the valid valley cells and 77% of the testable gorge corridor, so the count does not separate absorption from coverage loss. The adoption is therefore a judgment, made per flight without the post-event LiDAR. The zone contrast indicates absorption on both flights and is larger for the adopted valley spline, so it does not separate the two choices, which rest on different grounds. In the valley the spline is adopted for its lower held-out dispersion at 1 km blocks that exceed the 593 m residual range, at the cost in coverage quantified in Section 2.8; its valley mask also carries real 2017-to-2025 change, and the diagnostics of Section 3.1.5 make the adopted deposition term more likely an underestimate than an overestimate. In the gorge the regression is adopted because the sortie orthomosaic shows the corridor roads buried under fresh deposits (Section 3.2.2), so its stable cells carry real change; because the spline is undefined on 77% of the corridor; and because the 1 km blocks are a quarter of the 4.1 km residual range, which makes the spline's cross-validation there optimistic. Model averaging was not adopted, since the gorge spline is undefined on most of the corridor and an average would exist only on the remaining cells. The alternative is reported for both flights (Table 2; Section 3.2.3), thresholded with the adopted model's calibrated limit (the valley alternative also under its own limit, Section 3.1.5). For the two DSMs only the elevation-only regression was fitted.

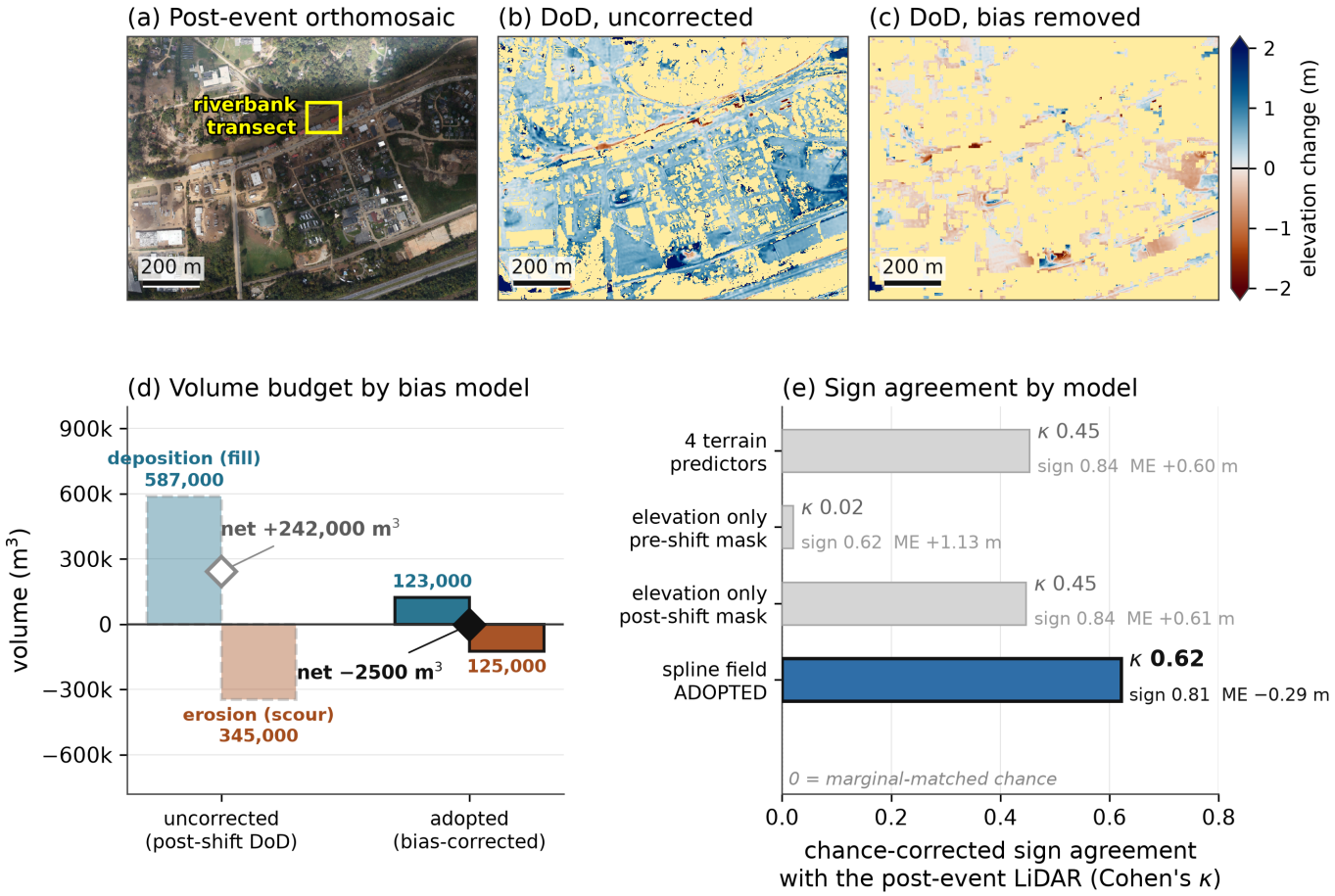


Figure 4. The bias correction determines the reported tally, Flight A0046B. (**a**) Post-event CAP orthomosaic of the Swannanoa commercial strip with the riverbank transect of Section 3.1.3 (yellow box). (**b**) Uncorrected and (**c**) bias-corrected DTM DoD over the same extent on identical color limits (pale yellow, no valid bare-earth value). (**d**) Flight-wide bare-earth tallies under the same calibrated local LoD: the uncorrected surface passes 7.5×10^5 significant cells against 1.62×10^5 after correction and reports five times the fill and a spurious net of $+2.4 \times 10^5$ m^3. (**e**) Bias models scored against the post-event LiDAR (Supplementary Table S2; the "pre-shift" fit is a superseded elevation-only fit on a stable mask screened before the shift, not a candidate); this is a consistency evaluation over changed ground, not the selector (Section 2.6), and it is confounded by cleanup, which removed deposits before the LiDAR flew and so favors the model that reports less deposition. Under the same limit the elevation-only model (intercept and slope) leaves 443,000 m^3 of deposition, and the spline's spatial structure and support restriction remove the rest.

2.7. Regional Screening

A coarse 10 m screen identifies where the 1 m processing should be concentrated. Both surfaces are averaged onto one aligned 10 m grid, co-registered with the road-based shift (Section 2.5), corrected for terrain-correlated bias, and restricted to cells with no vegetation returns. Open cells of the 10 m DoD (Section 2.4) with $|\text{DoD}| \geq 1$ m (r.dem.screen) form the Stage 1 screening zones and seed the buffered Stage 2 domain. On both flights the screen prioritizes rather than restricts the result: no cell enters a volume because it lies in a screening zone, since the gorge gap fill inside the zones never reaches the volumes (Section 2.3). Its recall against the flight-wide 1 m significance product is measured for A0046B in Section 3.1.4.

Table 2. Dual-surface volumetric change (m^3; gross terms rounded to three significant figures, nets below 10,000 m^3 to two) within the Swannanoa commercial strip, and the flight-wide bare-earth totals, under the calibrated local LoD. Nets are computed before rounding. DSM captures structures and canopy; DTM (bare earth) captures the land surface. Erosion is reported as negative and positive net indicates deposition (Supplementary Table S2 gives the flight-wide terms as unsigned magnitudes, without the isolated-cell removal). No flight-wide DSM total is reported. The last row is the alternative bias model, rescored without the isolated-cell removal (a sub-1% effect on the gross terms, Supplementary Tables S2 and S3), and gives the model-selection spread under the adopted limit (Section 3.1.5 gives it under the alternative's own limit). The uncorrected row is the post-shift DoD before any bias field. Stable-mask cells carry 42% of the A0046B deposition and 48% of the erosion (Section 3.1.5), and the commercial-strip rows include construction and grading that predate the storm (Discussion). Under 5% of the A0046B gross terms (3.4% of deposition, 4.7% of erosion) comes from cells above 775 m, the upper limit of the elevation band in which the bias correction was checked against the post-event LiDAR, whose footprint holds about 10% of the significant cells (Section 3.1.2).

Area of Interest	Surface	Deposition	Erosion	Net
Commercial strip	DSM	106,000	−60,900	+44,800
	DTM	3210	−3280	−66
Flight-wide	DTM	123,000	−125,000	−2500
Flight-wide, uncorrected (post-shift, no bias field)	DTM	587,000	−345,000	+242,000
Flight-wide, elevation-only model	DTM	443,000	−527,000	−84,400

2.8. Topographic Change Detection and Uncertainty Quantification

For each surface pair (Section 2.4), the DoD (Equation (2)) subtracts the 2017 LiDAR reference from the co-registered 2024 SfM surface, and change is significant where it exceeds the LoD (r.dem.lod) [70–74], calibrated so that 5% of the sloped, canopy-free stable-mask cells exceed it. That population includes real change (Section 3.1.5), so the limit is not a 95% confidence level for SfM error alone; on ground the post-event LiDAR shows unchanged, the chain flags 1.2% of cells (Section 3.3).

$$\mathrm{DoD}(x, y) = \mathrm{SfM}_{2024}(x, y) - \mathrm{LiDAR}_{2017}(x, y). \quad (2)$$

A global LoD applies one limit everywhere (Equation (3)), from the NMAD of a stable reference population [75], the road-PGCP cells for the DSM and the sloped stable-terrain mask for the DTM (per-flight limits in Supplementary Note S6). The published LiDAR error (Section 2.2) is already contained in those residuals, and the SfM term dominates.

$$\mathrm{LoD}_{95\%} = 1.96 \cdot \mathrm{NMAD}_{\mathrm{ref}}. \quad (3)$$

A local LoD replaces the single NMAD with a Gaussian-weighted windowed NMAD $\sigma_W(x, y)$ of the debiased stable-cell differences in a 21-cell window, combined with a flight-wide floor, and is computed only where the window holds at least 25 stable cells.

$$\mathrm{LoD}_{95\%}(x, y) = k_{95} \cdot \sqrt{\sigma_W^2(x, y) + s_{\mathrm{long}}^2} \quad \text{with} \quad s_{\mathrm{long}}^2 = \max\left(0,\ \sigma_{\mathrm{flight}}^2 - \mathrm{median}\,\sigma_W^2\right). \quad (4)$$

In Equation (4), the floor σ_{flight} is the stable-terrain dispersion of the debiased DoD, estimated by spatially blocked cross-validation and set to the larger of the in-sample and held-out values, so it is the held-out value for A0046B and the in-sample value for A0069AR (for A0046B bare earth the in-sample 0.20 m inflates to 0.46 m held out at 1 km blocks, both on the 4.28 million stable cells where the raw DoD is defined, each fold refitting the spline without the withheld blocks, against 0.72 m for the elevation-only regression; for A0069AR the adopted regression gives 0.66 m held out (0.44 to 0.83 m across folds) against 0.75 m in sample, and the spline 0.55 m held out against 0.32 m in sample, the deflation

that Section 2.6 warns of; held-out values are means of the five per-fold NMADs, which exclude between-fold offsets in the median and so can fall below the pooled in-sample value; the per-fold held-out median errors are −0.09 to −0.19 m for the A0046B spline, consistently negative as the over-correction of Section 3.1.2 implies, and −0.18 to +0.08 m for the regression, and adding each fold's median error to its NMAD in quadrature leaves the ranking unchanged at both block sizes on both flights (1 km: 0.48 against 0.73 m for A0046B, 0.59 against 0.73 m for A0069AR); the A0046B floor is therefore a lower bound, and the 1 km gorge blocks are a quarter of that flight's 4.1 km residual range). The realized constants are floors of 0.46 m (A0046B bare earth, held out), 0.75 m (A0069AR bare earth, in sample), and 2.14 and 0.80 m for the DSMs, with k_{95} of 1.56, 2.68, 3.69, and 2.65 (Supplementary Note S6). Because k_{95} is calibrated on the in-sample debiased residuals, the 5% exceedance holds in sample, and the cross-validated floor raises the final A0046B limit by about 14% relative to a fully in-sample calibration (mean local limit 0.76 against 0.67 m, Supplementary Table S7), not by the factor of 2.3 between the two floors. Only its long-wavelength excess s_{long} enters, since the window resolves the short-wavelength part [76–79]. The multiplier k_{95} is the empirical stable-cell 95th percentile of $|\Delta h|/\sqrt{\sigma_W^2 + s_{\mathrm{long}}^2}$ rather than the Gaussian 1.96, which understates the tail of leptokurtic residuals [75]; the realized values exceed 1.96 except for the A0046B bare earth (1.56), whose blocked cross-validated floor already overstates the short-wavelength dispersion (Supplementary Note S6).

The test is defined only where stable terrain is within window reach, and for the A0046B bare earth that restriction acts in two stages. Of the 16.6 million observed bare-earth cells, the support of the spline bias field retains 6.5 million, and window reach leaves 3.54 million testable cells (21%), so most of the A0046B coverage loss comes from the spline's support rule (Section 2.6), which the elevation-only model would not impose. Testable cells are 53.9% of observed DSM cells for A0046B, and in the open-ground A0069AR corridor 55.5% of observed bare-earth cells and 57.3% of observed DSM cells. Cells beyond reach are reported as observed but untestable (Figure 2), so every reported volume is a lower bound with respect to coverage; within the testable domain the thresholded terms also carry a systematic term of about 5% of each valley gross term, identified from the check cells, and a gorge term of about 7.5% set by the intercept, both lowering deposition and raising erosion (Sections 3.1.2 and 3.2.3), and a false-positive component (Section 3.3). The 21-cell window is fixed a priori and drives coverage rather than the limit. Across the 5- to 81-cell sweep the calibrated mean limit varies only 0.66–0.87 m for A0046B (1.9–2.2 m for A0069AR) while the testable cells change 14-fold and the gross volumes grow by roughly 12- and 18-fold (A0046B erosion and deposition) and 20- and 80-fold (A0069AR) (Supplementary Tables S3 and S4 and Note S6). No window can decorrelate the residuals, whose fitted semivariogram ranges of 593 m in the valley and about 4.1 km along the gorge (Supplementary Table S6) sit far above every candidate window, so the spatially correlated error is carried by the volumetric propagation (σ_V, Section 3.1.5).

The dispersion is estimated on stable surfaces and applied to changed ones with larger error. The post-event LiDAR bounds that inflation for A0069AR but not for A0046B, whose changed-cell residual is dominated by cleanup. For A0069AR the changed-cell dispersion is 1.20 times the stable value at a 1 m change threshold (1.27 at 0.5 m); because that dispersion also contains recovery change, the factor is an upper bound on the error inflation, and under a limit inflated by 1.2 the gorge positive term falls from 8.4×10^4 to 5.0×10^4 m^3 and remains resolved at about $3.0\,\sigma_V$ (RMS-based, Supplementary Note S6). The flight-wide volumes are stable under a reallocation of the limit between floor and multiplier (Supplementary Table S7). The masked DoD (r.dem.change) retains change where $|\mathrm{DoD}| > \mathrm{LoD}_{95\%}$, with isolated significant cells (no significant 8-neighbor) removed before any volume is tallied, and a continuous confidence surface (r.dem.errprop) from the

same stable-cell σ_{DoD} classes cells by z-score into 68–99% classes, read as relative because the errors are spatially autocorrelated (Supplementary Note S6).

2.9. Volume and Geomorphic Change Assessment

Flight-wide erosion and deposition volumes are the cell sums of the LoD-thresholded DoD (r.dem.change) per surface within the masks of Section 2.4, and because the bias correction of Section 2.6 precedes thresholding, every volume, significance product, and z-score derives from the same bias-corrected surface. Site-specific volumes clump connected significant cells (r.clump, minimum 10 cells) and integrate the DoD over each feature (r.volume). Consistent with the propagated uncertainties, volumes are reported to at most three significant figures (gross terms at flight scale to the nearest 1000 m^3, nets below 10,000 m^3 to two significant figures) and error and dispersion statistics to at most two decimals in meters, with supplementary tables carrying one more digit where a sensitivity comparison needs it.

3. Results

3.1. Flight A0046B: Swannanoa Valley

3.1.1. A0046B Photogrammetry Processing Summary

Flight A0046B (land-surface parameters in Supplementary Figure S2) aligned 1468 of 1515 photos over 78.4 km^2 (RMS reprojection error 0.547 pixels, flight report; block diagnostics in Supplementary Table S14), and its 7.95 cm orthomosaic carries exposure artifacts from variable camera settings (Section 4.1).

3.1.2. Post-Storm Surface Accuracy

The road-PGCP median vertical shift (Section 2.5) removed a 5.37 m offset from the DSM and 5.03 m from the DTM (whole-scene DSM statistics before and after the shift in Supplementary Table S1). On the sloped stable-terrain mask of Section 2.6 it reduced the DTM mean error from +5.55 to +0.52 m and the RMSE from 5.74 to 1.55 m, and left the DSM at a mean error of +0.32 m and an NMAD of 2.12 m (Supplementary Table S12). A seven-fold cross-validation of the shift on 250 m spatial blocks of canopy-free road control cells (cells within 5 m of the centerlines that the SfM cloud also classifies as road), without the post-event LiDAR, gives a held-out RMSE of 0.34 m ($n = 4.7 \times 10^4$), 1.13 times the in-sample value. That control set is defined separately from the 700,095-cell road-PGCP population that sets the shift (cells within 2 m of the centerlines, post-shift NMAD 0.64 m, Supplementary Figure S11a and Table S5), so 0.34 m describes the stability of the shift, not the accuracy of the control as a whole. The remaining half meter is the elevation-dependent residual (Figure 3a). The elevation-binned check of Figure 3b uses independent check cells, open cells that the post-event LiDAR shows unchanged ($|\text{LiDAR change}| < 0.25$ m, about twice the combined inter-epoch RMSE of Section 2.2, n = 824,056, 21% of them also bias-fit cells), with the residual taken against the post-event LiDAR, so it tests the correction against a reference the fit never saw; the LiDAR footprint holds about 10% of the A0046B significant cells. Its ten equal-count bins have medians of 653 to 703 m, but the cells reach 890 m (35,974 above 705 m, 2590 above 750 m). Re-binned in fixed 25 m bands holding at least 1000 cells, the prediction exceeds the observed residual by 0.15 and 0.13 m below 700 m, by 0.05 m at 700 to 725 m, and by −0.06 and +0.01 m at 725 to 775 m, so the over-correction is confined to the valley floor. Above 775 m, the upper limit of that support, lie 4.8% of the 162,288 significant bare-earth cells, carrying 3.4% of the gross deposition and 4.7% of the gross erosion. Weighted by where the significant cells lie, the in-band gap is a systematic term of about 1.3×10^4 m^3 on the net, about 1.6 σ_V (RMS-based, Section 3.1.5), in the direction

of over-correction: it lowers the deposition term by about 6.5×10^3 m^3 (5.3%) and raises the erosion term by about 6.2×10^3 m^3 (5.0%); this linear estimate omits cells that the shift carries across the detection limit, so the effect may be larger. For A0069AR the check cells (n = 222,204) reach 812 m, with gaps of both signs up to 0.55 m in bands holding at least 1000 cells up to 500 m; above 500 m lie 27% of its significant cells, 14% of the deposition, and 30% of the erosion. Weighted by where the gorge significant cells lie, its gaps of both signs nearly cancel ($+0.4 \times 10^3$ m^3), with an absolute bound of 7.7×10^3 m^3, under half of σ_V (RMS-based).

In the consistency evaluation of Section 3.3, where the SfM detects significant DSM change its sign agrees with the independently measured LiDAR-to-LiDAR change on 79.3% of cells, and for the DTM on 80.8%. Both DoDs are differenced against the same 2017 LiDAR, so their errors are positively correlated and agreement is inflated.

3.1.3. Spatial Patterns of Topographic Change

The uniform global DSM LoD, 1.96 times the road-control NMAD, is 2.09 m. The calibrated local LoD (Section 2.8) differs from it in reference population and multiplier as well as in spatial variation: at median window dispersion Equation (4) gives $k_{95}\,\sigma_{\text{flight}} = 3.69 \times 2.14 = 7.9$ m, and across the flight the limit ranges from 6.5 m to 192 m at structure edges (mean 10.6 m), reaching tens of meters over the buildings of the Swannanoa commercial strip. Of the 10.2 million DSM cells the global limit flags as significant, 92.6% are not significant under the local test: 87.2% of the 5.9 million where the local limit is defined, and all of those beyond window reach (Supplementary Figure S17 shows the commercial strip).

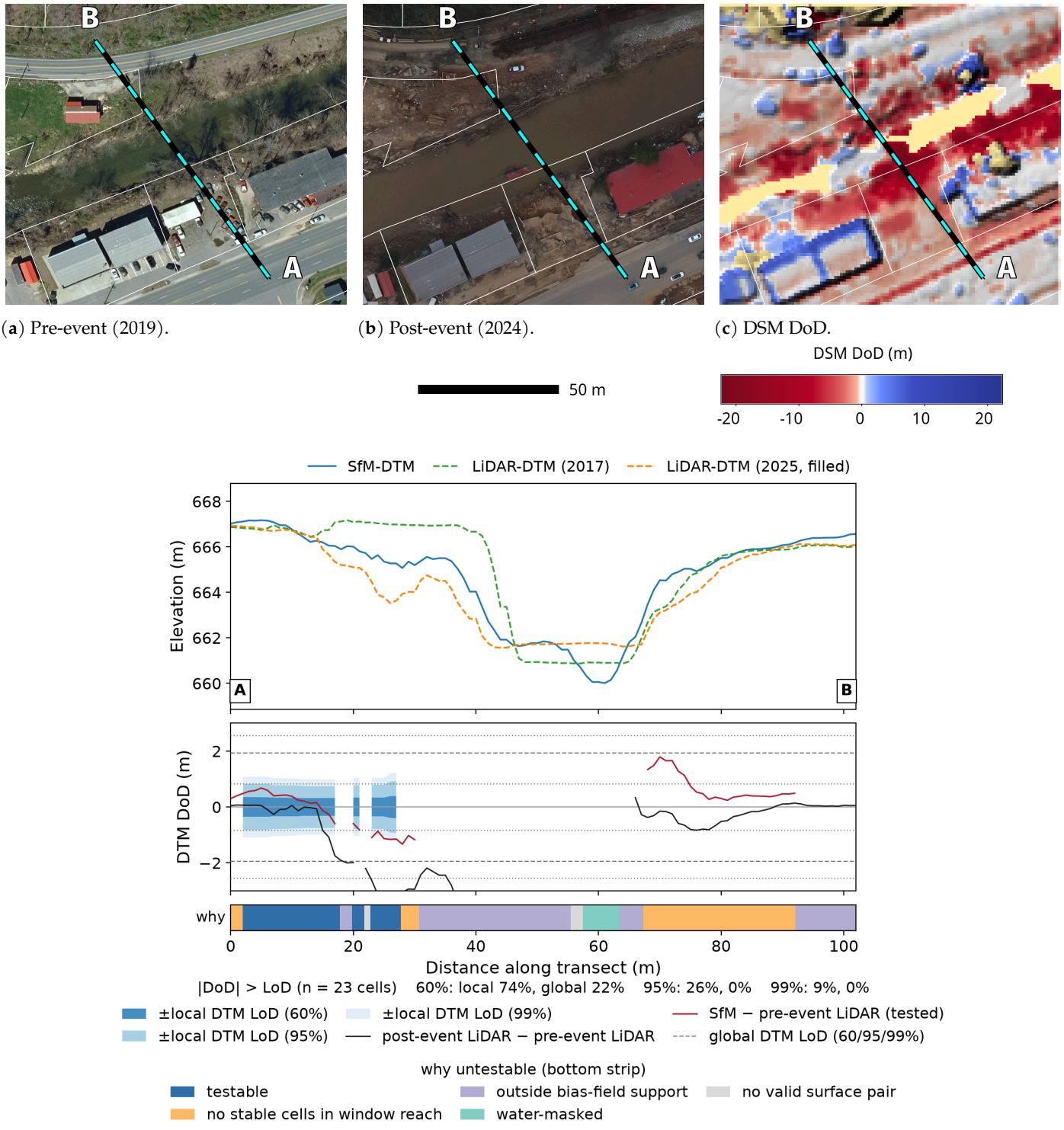
Figure 4a locates the riverbank transect inside the commercial strip. Sedimentation covers the flat urban landscape, such as parking lots and grassy areas, while erosion dominates the banks of the Swannanoa River (Figure 5c), and the profile resolves it against all three elevation epochs (Figure 5d). A field with localized raised overbank patches (Supplementary Figure S12), a tributary reach (Supplementary Figure S13), and a landslide above the Grovemont neighborhood (Supplementary Figure S15) are profiled the same way.

3.1.4. Regional Screening Result

The 10 m regional screen (Section 2.7) flagged 48,568 cells, 6.5% of the 74.2 km^2 screening footprint. A buffered Stage-2 domain built from these flags would have cut the processed area by 42% (retaining 4.3×10^7 of 7.4×10^7 cells) while capturing 98.8% of the significant bare-earth cells (86.4% of the DSM cells, and 81.5 to 87.6% across the 0.5 to 2.0 m thresholds, Supplementary Note S8) and 99.0% of their volume at the 1.0 m screening threshold (omitted volume about 2600 m^3, about 1% of the gross budget). Recall moves from 98.9% to 96.9% as the threshold rises from 0.5 to 2.0 m while the area reduction grows from 41 to 48% (Supplementary Table S10). The 50 m buffer around the flagged cells, not the raw flags (which alone capture 50.9%), carries this recall.

3.1.5. Volumetric Change by Area of Interest

Volumetric change was integrated for both surfaces under the calibrated local LoD (Section 2.8) and the canopy check of Section 2.4 (Table 2). Every tally measures 2017-to-sortie change within the testable domain and is a lower bound in coverage. An image check dates a minority of the valley change and just under half of the gorge change to the sortie (Discussion). Within the commercial strip the DSM net of +44,800 m^3 registers lost structures and vegetation as well as sediment, while the DTM passes only about 3200 m^3 in each direction.



(**a**) Pre-event (2019). (**b**) Post-event (2024). (**c**) DSM DoD.

(**d**) DTM profile along A–B.

Figure 5. Riverbank transect A–B on the Swannanoa River, Flight A0046B, located in Figure 4a. (**a**) Pre-event 2019 NC OneMap orthoimagery [38]. (**b**) Post-event CAP SfM orthomosaic. (**c**) Unthresholded debiased DSM DoD over the SfM DSM hillshade; the color bar spans the full value range and pale yellow is no data. Panels (**a–c**) show parcel boundaries [43] and share the scale and color bars; all panels are north up. (**d**) The three DTM epochs along A–B, the DoD with the local LoD at 60, 95, and 99% (60% marks sub-threshold change only) and the global LoD, the LiDAR-to-LiDAR change, and why cells are untestable; the 2025 LiDAR DTM is gap-filled for display, and flat 2017 segments are hydro-flattened water.

Flight-wide the DTM records 125,000 m^3 of scour against 123,000 m^3 of deposition over 162,000 significant cells, a net of −2500 m^3. The uncorrected difference returns 587,000 m^3 of apparent deposition against 345,000 m^3 of scour, because the post-shift residual is positive and spatially structured and integrates as spurious deposition. The correction removes roughly four fifths of the apparent deposition and the spurious +242,000 m^3 net (Figure 4), so it determines the volumetric result rather than refining it. Of that reduction the elevation-only model (intercept and slope) accounts for the step from 587,000 to 443,000 m^3 and the spline for the step from 443,000 to 123,000 m^3 (Table 2, uncorrected and alternative rows, both under the adopted limit). That second step, about 70% of the reduction, combines spatial structure that no elevation term represents with the spline's support restriction, which leaves the field undefined on 61% of the valid cells; neither part is constrained by the mechanism diagnostics of Section 2.6, and neither transfers to another flight (flight-wide maps before and after correction in Supplementary Figures S3 and S4). Three stable-ground diagnostics point the same way: the bias field over-predicts the check-cell residual on the valley floor (Section 3.1.2), the debiased residual against the post-event LiDAR on those cells is −0.19 to −0.04 m in every bin (Figure 3b), and the spline lowers its Stage 1 deposition zones by 0.80 m on average relative to the elevation-only model (0.84 m relative to stable ground). The adopted deposition term is therefore more likely an underestimate than an overestimate. The volume of that zone shift is not fully counted. The 3314 significant cells that remain in those deposition zones are lowered by 0.90 m on average relative to the regression, about 3.0×10^3 m^3, but cells the shift pushes below the limit lose their whole DoD and are not in that figure, so it is a lower bound; the field difference averages 0.80 m over all 70,471 zone cells, about 5.6×10^4 m^3, which gives the scale. Stable-mask cells are not excluded from the tally, and by the calibration 5% of them exceed their limit (77,557 of 1.55 million A0046B stable cells inside the LoD domain); they hold 77,191 of the 162,288 significant cells, with 51,000 m^3 of deposition and 61,000 m^3 of erosion (42% and 48% of the gross terms), leaving 71,000 and 65,000 m^3 off the mask (A0069AR: 18,868 of 47,178 cells, 21,000 and 33,000 m^3, leaving 63,000 and 43,000 m^3). They are not noise. Inside the post-event LiDAR footprint their sign agrees with the LiDAR-to-LiDAR change on 88% (A0046B) and 89% (A0069AR) of cells, against 75% and 91% for significant cells off the mask (agreement inflated by the shared 2017 reference, Section 3.1.2), and the median LiDAR change on them is 0.81 and 2.03 m. The sloped, canopy-free stable mask therefore carries real 2017-to-2025 change, the calibrated 5% exceedance is mostly real change, and the limit calibrated on it is conservative.

Two uncertainty classes accompany these volumes. The random volumetric uncertainty, conditional on the adopted bias model and propagated with the measured spatial correlation of the residuals [78,80,81], is $\sigma_V \approx 6.2 \times 10^3$ m^3 (median per-cell σ of the propagated error surface over the significant cells ≈0.41 m; with the RMS of 0.53 m the same estimator gives 8.0×10^3 m^3, the conservative value used for comparisons below) from a spherical semivariogram of the debiased stable-cell residuals with a 593 m range (Supplementary Table S6). The estimator is $\sigma_V = \sigma A n / \sqrt{n_{\text{eff}}}$ with $n_{\text{eff}} = 1/\bar{\rho}$, the reciprocal of the mean pairwise correlation over the significant cells under the fitted model ($n_{\text{eff}} = 116$ here and 11 for A0069AR), which places σ_V between the fully independent (1.7×10^2 m^3) and fully correlated (6.7×10^4 m^3) limits, and a ±50% perturbation of the range moves σ_V only between 4.4×10^3 and 7.7×10^3 m^3. The 593 m range is fitted on in-sample spline-debiased residuals and may understate long-wavelength correlation, for which the fully correlated 6.7×10^4 m^3 is the bound; $\bar{\rho}$ is taken from the fitted model including the nugget, and one σ_V, computed over all significant cells, is quoted for the net and for each gross term. The net (−2500 m^3) is within one σ_V of zero; with the identified systematic term of Section 3.1.2 applied it would be about $+1.0 \times 10^4$ m^3, about 1.3 σ_V, so it is indistinguishable from zero at

two σ_V either way, and the gross scour and fill terms, not their difference, carry the finding. Model-selection uncertainty is not contained in σ_V. The headline volumes are conditional on the spline bias model, adopted without the post-event LiDAR (Section 2.6). Between the two candidates of Supplementary Table S2, the adopted spline and the elevation-only model, the flight-wide gross terms span 1.2×10^5 to 4.4×10^5 m^3 of deposition and 1.3×10^5 to 5.3×10^5 m^3 of erosion (Table 2), a 3.6- to 4.2-fold spread under the detection limit calibrated on the adopted model, which dwarfs σ_V. Thresholded instead with its own calibrated limit (floor 0.72 m, k_{95} 2.20) on its own, larger support, the alternative gives 1.1×10^6 m^3 of deposition and 4.1×10^5 m^3 of erosion (without the isolated-cell removal), 3.3- to 8.7-fold the adopted terms, so the quoted spread is not a bound in either direction; its size depends on whose limit and support are used. The excluded four-predictor regression falls inside the deposition span (427,000 m^3) and just above the erosion span (555,000 m^3), and the larger deposition in Supplementary Table S2 belongs to a superseded elevation-only fit on a stable mask screened before the shift (Supplementary Note S5), not to a candidate. In-channel transport is omitted, since only 2% of the buffered channel and water cells are testable (0.1% in the gorge corridor), so the total is not a sediment budget of the river system.

3.2. Flight A0069AR: Hickory Nut Gorge

3.2.1. A0069AR Photogrammetry Processing Summary

Flight A0069AR aligned 1395 of 1443 photos over 77.6 km^2 (RMS reprojection error 0.496 pixels, flight report; block diagnostics in Supplementary Table S14), and the co-registered terrain and its land-surface parameters are shown in Supplementary Figure S5. At 1 m the DSM fills 34% of its bounding box, and that coverage limit, not the co-registration, confines change detection to the open-ground corridor.

3.2.2. Post-Storm Surface Accuracy in a Forested Gorge

Of the 77.6 km^2 mapped, 96% is forested (mean LiDAR canopy height 22 m) and only 4% is open ground (canopy < 2 m) along the Rocky Broad River corridor and Lake Lure, which is 5.5% of the 59.6 km^2 flight hull, the convex hull of the camera stations inside the mapped extent, used for the exclusion accounting (Supplementary Table S11). Under intact forest the SfM bare-earth "DTM" rides near the canopy, so change detection is restricted to the open-ground corridor and no whole-footprint volumes are reported (Supplementary Figure S6 and Note S1).

Independent per-surface road-median shifts disagree here (+4.05 m bare earth, +3.71 m canopy). The decision to share one shift used sortie-epoch evidence alone: the CAP orthomosaic shows the corridor roads buried under fresh deposits, so the bare-earth road median was treated as contaminated and the canopy-surface median was applied to both surfaces. The road residuals agree. Resampling NCDOT routes leaves the bare-earth median poorly determined (two-stage bootstrap standard error 2.0 m over 29 routes, against 0.14 m for the canopy-surface median over 51 routes), and 55 of its 171 road segments of 250 m depart from the median of the segment medians by more than three NMAD (Supplementary Note S13). The gap does not itself diagnose the deposits. On open road cells a deposit raises the maximum-Z and minimum-ground SfM surfaces alike, so the canopy-surface median is not free of it either, and the valley shows a gap of the same size with the opposite sign (DSM +5.37 m, DTM +5.03 m) where the roads are not buried. Gaps of this size can come from the surface definitions alone: the 2017 first-return DSM includes overhanging canopy on road cells that are not filtered for canopy, the bare-earth reference is the interpolated OPR DTM, and the SfM surfaces are maximum-Z and minimum-ground bins. The shared shift is therefore a convention prompted by the imagery rather than a measured correction, and for a third flight it is an analyst heuristic: when the imagery shows the roadbed covered,

apply one road median to both surfaces. It would not apply to A0046B, whose roads are not covered. After the shared shift the sloped stable-mask bare-earth mean error is +0.67 m (NMAD 1.32 m, Supplementary Table S13), on a hull-wide mask that includes cells under canopy that the SfM classifier labeled ground. The three bare-earth dispersions quoted for this flight describe different comparisons: 1.32 m is the spread against the 2017 reference on the hull-wide 1.96 million-cell sloped stable mask (numerically equal to, but distinct from, the 1.32 m RMSE of Table 3 against the post-event LiDAR), the 0.75 m floor is the in-sample NMAD of the debiased DoD on the 412,513 stable cells inside the open-ground corridor, and the 0.82 m of Table 3 is the error against the post-event LiDAR on stable terrain. The choice is bounded in three ways. On canopy-free control the bare-earth median is stable (held-out RMSE 1.21 m from a spatially blocked seven-fold cross-validation on $n = 2300$ canopy-free control cells, 2% above the in-sample value), even though it varies across routes. The reported volumes do not depend on the shift beyond the centering of the residual screen, because the elevation-only bias model fitted downstream has a free intercept that absorbs any uniform shift. And the choice is made without the post-event LiDAR.

Table 3. Comparison of the co-registered SfM surfaces with the post-event LiDAR (SfM − LiDAR), stratified by terrain over the full LiDAR footprint. The stable stratum is the accuracy validation; the other strata include real post-sortie change and are temporal comparisons. Stable = the sloped stable-terrain mask of Section 2.6 (slope 5 to 50°, zero vegetation returns, outside the 15 m hydrography buffer, |SfM − 2017 LiDAR| < 5 m) inside the post-event LiDAR footprint, n = 1,008,335 (A0046B) and 442,494 (A0069AR), of which 574,485 and 105,957 cells lie where the raw DoD is defined (NMAD 0.48 and 0.52 m) and the rest outside it, for A0069AR partly under canopy the SfM classifier labeled ground; canopy classes from the 2017 LiDAR canopy height. The DSM stable stratum holds 993,403 (A0046B) and 385,780 (A0069AR) cells. Statistics are for the co-registered surfaces before bias correction; the bias-corrected values are given in Section 3.3. ME, mean error; MED, median error; NMAD, normalized median absolute deviation.

Flight	Stratum	n	ME (m)	MED (m)	RMSE (m)	NMAD (m)
A0046B	DTM stable	1.0×10^6	+0.73	+0.50	1.43	0.68
	DTM open ground	3.5×10^6	+3.42	+0.48	8.16	0.72
	DTM canopy 2–10 m	2.2×10^6	+7.72	+3.91	11.47	5.89
	DTM canopy >10 m	2.0×10^6	+13.09	+13.83	16.25	12.42
	DSM stable	9.9×10^5	−0.37	+0.18	6.72	1.03
A0069AR	DTM stable	4.4×10^5	+0.55	+0.35	1.32	0.82
	DTM open ground	3.9×10^5	+0.60	+0.13	2.59	0.53
	DTM canopy 2–10 m	2.8×10^5	+2.45	+0.71	5.63	1.30
	DTM canopy >10 m	1.8×10^6	+8.20	+2.63	12.89	4.64
	DSM stable	3.9×10^5	−2.10	−0.11	7.21	0.93

3.2.3. Open-Ground Geomorphic Change

Over the 1.3 km^2 valid bare-earth DoD footprint of the open corridor (1.2 km^2 of it inside the camera-station hull of Supplementary Table S11, of which 0.65 km^2 is testable), the LoD-masked bare-earth DoD (mean local limit 2.1 m, 2.2 m for the DSM) records 84,000 m^3 of positive change against 76,000 m^3 of erosion over 47,000 significant cells; of the positive term, about 7.3×10^4 m^3 is deposition on land and 1.05×10^4 m^3 lies on the 2017 Lake Lure surface and is unattributed (Section 3.2.4). The residuals correlate over kilometers along the gorge (exponential fit, practical range ~4 km), giving $\sigma_V \approx 1.5 \times 10^4$ m^3 (median per-cell $\sigma \approx 1.1$ m, RMS 1.2 m giving 1.7×10^4 m^3; 1.1×10^4 to 1.9×10^4 m^3 under a ±50% range perturbation). The net ($+8.1 \times 10^3$ m^3, about 0.5 σ_V RMS-based and about 1.2 σ_V with the intercept term below applied) remains unresolved and changes sign across the window-size sensitivity (Supplementary Table S4). The gross positive term (5.0 σ_V, RMS-based) and its land deposition part (4.4 σ_V) are resolved and carry the finding, conditional on the elevation-only model of Section 2.6 (flight-wide maps before and after correction in

Supplementary Figures S7 and S8). Model selection is the larger uncertainty class in this flight. The spline is defined on only 168,535 of the 731,946 testable cells; on those shared cells and under the adopted limit it reports 5100 m^3 of deposition and 3300 m^3 of erosion against 19,000 and 15,000 m^3 for the adopted regression, and 71,000 m^3 of the regression's 90,600 m^3 of deposition lies where the spline is undefined (rescored without the isolated-cell removal, Supplementary Table S2). The applied elevation-only model reduces in practice to its intercept: fitted on the corridor's 412,513 stable cells, it has a slope of −0.024 m per 100 m and an intercept of +0.25 m at the mean elevation of 402 m (Supplementary Note S5). That free intercept absorbs the +0.25 m mean of the raw DoD on those cells (the hull-wide +0.67 m of Supplementary Table S13 includes cells under canopy). That mean is about what the choice of the canopy-surface shift alone predicts: under the bare-earth shift, 0.34 m higher, it would be about −0.09 m, so it does not measure deposits. If the corridor's stable cells do carry deposits, as the buried roads suggest, the correction references the corridor to a datum inside them. The size of that effect is not measured; as a scale, if the whole intercept were deposit, removing it would lower deposition and raise erosion by 0.25 m per cell, which over the 47,178 significant cells is 1.2×10^4 m^3 on the net (6.1×10^3 m^3, 7.3%, of the deposition term and 5.7×10^3 m^3, 7.5%, of the erosion term), within one σ_V, as a linear approximation that omits cells the shift carries across the detection limit, so the effect may be larger; over the 731,946 testable corridor cells it would be 1.8×10^5 m^3 if applied without a threshold.

As a consistency check on the closure cells of Section 3.3, the A0069AR significant bare-earth cells agree in sign with the post-event LiDAR change over 90.0% of 17,024 cells, with a residual of −0.29 m mean (−0.48 m median) dominated by reconstruction fill the LiDAR measured that did not exist at the sortie, and by positive clusters where sortie-time deposits were removed before the LiDAR flew. Through Chimney Rock village the fill stands +2 to +4 m above the storm-time SfM surface (over 187 m of the 298 m road profile it exceeds the 0.82 m stable NMAD, by +2.4 m on average, Supplementary Figure S14).

3.2.4. Lake Lure Reach

A raft of floating woody and structural debris accumulated at the gorge mouth on Lake Lure (Supplementary Figure S16). The open-ground rule admits the lake, and 3822 significant cells on the hydro-flattened 2017 lake surface (298.26 m), 3692 of them outside the flowline buffer, enter the gorge positive term with 1.05×10^4 m^3 (13% of it, mean +2.8 m) and are reported as unattributed change. The SfM surface there may record delta sediment, a higher water level, or the emergent surface of floating debris, which the data cannot separate. We document the raft but do not quantify it as a separate volume, since the SfM surface records only its emergent upper surface, a floating body offers no stable basal reference, and its clearance before the early-2025 LiDAR leaves the rapid SfM surface as its only elevation record. Deposition on the surrounding land at the Rocky Broad inflow and Morse Park (sites P1 and P2; change residual in Figure 6, DoD in Supplementary Figure S8) is resolved against the pre-event LiDAR, itself a lower bound because material below the waterline is not recovered. The ~7.6×10^5 m^3 later removed from Lake Lure [32] is different material in a different place and gives context, not corroboration.

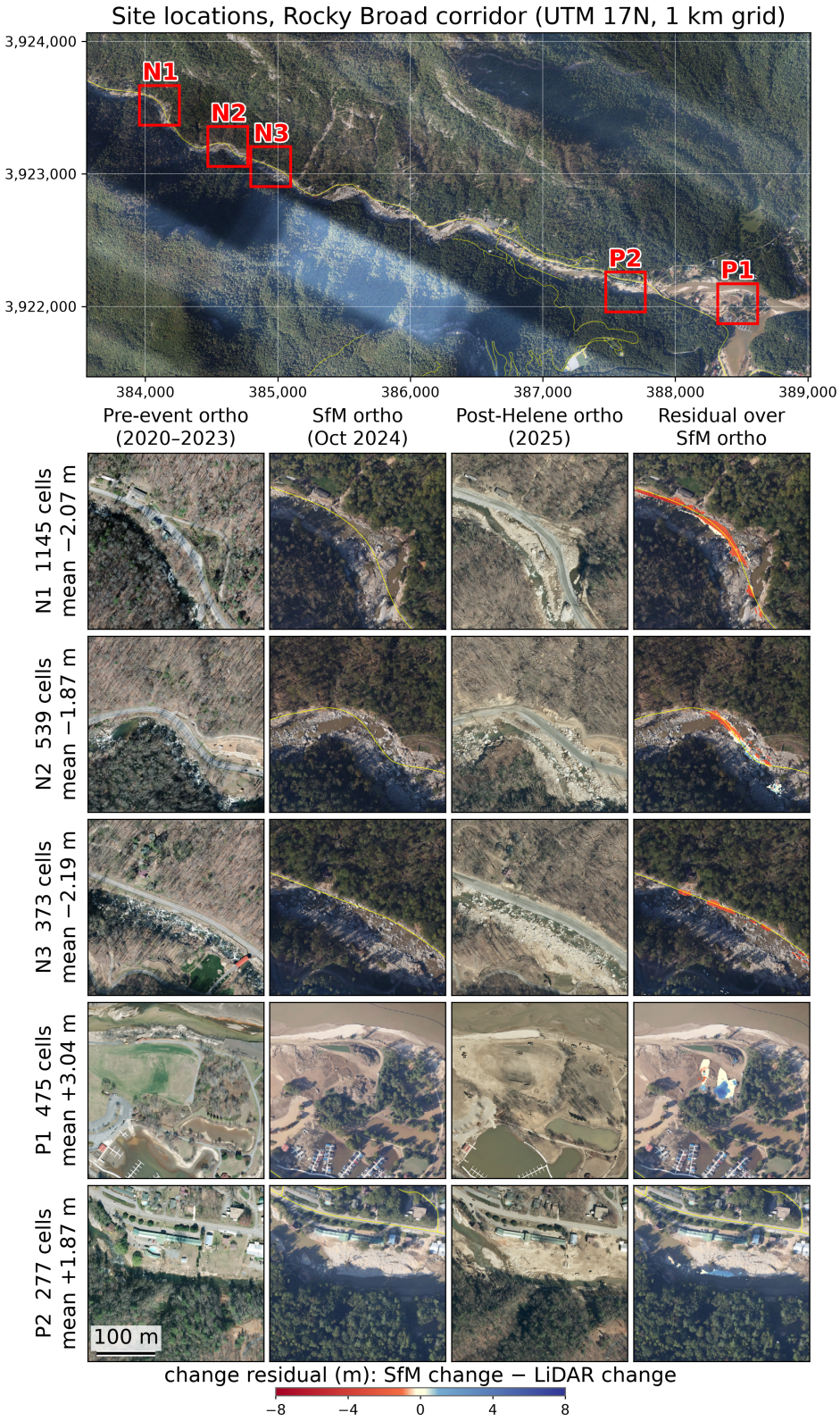


Figure 6. Change residual hotspots in the A0069AR corridor. Top: locator (UTM 17N). Columns: pre-event orthoimagery (NC OneMap 2020–2023 [39]), the October 2024 CAP SfM orthomosaic, post-Helene 2025 orthoimagery (NC OneMap [40]), and the SfM orthomosaic with the change residual; yellow lines are the NCDOT road centerlines. Sites N1–N3 trace the destroyed road and channel below Chimney Rock; P1 and P2 sit at the Lake Lure inflow. Row labels give each site's cell count and mean residual; the residual color bar is linear.

3.3. Validation Against Independent Post-Event LiDAR

The post-event LiDAR of Section 2.2 entered no fit, since the co-registration, bias model, detection-limit window, and A0069AR shared shift follow criteria computable without the post-event LiDAR (Sections 2.6, 2.8 and 3.2.2), so it serves as an independent test of both flights. Table 3 evaluates the co-registered surfaces before the bias correction, so its mean errors still contain the terrain-correlated bias that Section 2.6 removes from every reported volume. Throughout the paper, "validation" is reserved for this stable-terrain accuracy comparison, where the mask assumes no change. Comparisons over changed ground mix SfM error with real change between the sortie and the LiDAR flight, and are read as an independent consistency evaluation, a temporal comparison rather than an error statistic. On that basis, over the significant cells inside the post-event LiDAR coverage (the closure cells), the sign of the A0046B debiased DoD agrees with the LiDAR-to-LiDAR change on 79.3% of DSM cells (n = 98,888) and 80.8% of DTM cells (n = 16,549; for A0069AR 90.0% of 17,024 DTM cells with a −0.29 m mean residual, Section 3.2.3), with median change residuals of +1.81 m (DSM) and −0.50 m (DTM).

On stable terrain the DTM NMAD is 0.68 m (A0046B) and 0.82 m (A0069AR), and 0.48 and 0.52 m on the stable cells where the raw DoD is defined (574,485 and 105,957 cells; mean errors +0.43 and +0.19 m), with full-stratum mean errors of +0.73 and +0.55 m (after the shared shift the A0069AR open-ground median difference is +0.13 m). After bias correction, on the 207,590 A0046B stable cells where the bias-corrected DoD is defined, which belong to the stable population the spline was fit to and so measure agreement on the fit population rather than held-out skill (held-out NMAD 0.46 m, Section 2.8), the residual against the post-event LiDAR is NMAD 0.22 m, mean error −0.03 m, and RMSE 0.34 m, against 0.46 m, +0.36 m, and 0.60 m before correction on the same cells; for A0069AR (105,957 cells) the correction, effectively an intercept, leaves the NMAD at 0.52 m and moves the mean error from +0.19 to −0.07 m. The co-registered stable error degrades by factors of 18 and 5.6 (from the unrounded values) under forest taller than 10 m (NMAD 12.4 and 4.6 m). The median and NMAD are the appropriate DSM measures, since canopy edges, regrowth, and rebuilt structures in the 2025 returns enter a mean and not a median. The post-event LiDAR also checks the calibrated threshold (Section 2.8). Where the LiDAR-to-LiDAR change is below 0.15 m (about 1.2 times the combined inter-epoch RMSE, stricter than the 0.25 m of the elevation check, chosen to test false positives), the full chain flags 1.2% of cells on both flights (4607 of 369,697 A0046B cells and 1440 of 124,946 A0069AR cells) as significant, below the 5% calibrated on the stable mask, which carries real change (Section 3.1.5). Inside the LiDAR footprint the flagged unchanged cells carry 4800 (A0046B) and 6400 m^3 (A0069AR), with mean |DoD| of 1.05 and 4.45 m. Scaling the flag rate and the mean |DoD| to every testable cell (3.54 million for A0046B, and 731,946 for A0069AR, where the gorge limit and the corrected DoD are both defined, including corridor cells outside the camera-station hull) gives an upper bound on the flight-wide false-positive component of about 4.6×10^4 and 3.8×10^4 m^3, about 19% and 24% of the summed gross terms; it is an upper bound because not all testable cells are unchanged, and it assumes that the flag rate measured inside the post-event LiDAR footprint, which holds about 10% of the A0046B significant cells, applies across the testable domain. The flagged cells lean to erosion in the valley (1311 deposition and 3296 erosion cells, 1700 and 3200 m^3) and to deposition in the gorge (867 and 573 cells, 4500 and 1900 m^3), so the scaled bounds are 1.6×10^4 and 3.0×10^4 m^3 on the valley deposition and erosion terms (13% and 24%) and 2.6×10^4 and 1.1×10^4 m^3 on the gorge terms (31% and 15%). In the worst case the gorge positive term falls to about 5.8×10^4 m^3, still more than 3 σ_V. This component runs against the lower bound in coverage.

4. Discussion

The bare-earth accuracy reported here holds on unchanged, unvegetated terrain within reach of the valley-floor control, not on the impacted hillslopes where much of the debris mobilization and infrastructure loss was concentrated. Only 54% of the observed DSM footprint, and 21% of the bare-earth footprint, is testable (Section 2.8); for the A0046B bare earth most of the loss comes from the spline field's support rule rather than distance from stable control. The testable bare-earth domain covers 5.6% of the Swannanoa flight hull (21.3% of its DoD footprint) and 1.1% of the gorge hull (55.5% of its open-ground footprint, Supplementary Table S11). Within canopy below 2 m, 85% (A0046B) and 80% (A0069AR) of cells are still excluded, by low ground-point density in the valley and by missing bare-earth reconstruction and the open-ground restriction in the gorge, so the testable domain covers 15 to 20% of the open ground in each hull. Canopy taller than 10 m covers 27.5% and 86.6% of the two hulls and is essentially fully excluded, the same canopy that hid landslide source areas from the imagery used in the Helene response [9]. Of the 186 USGS Hurricane Helene landslide inventory [82] points inside the two flight hulls, one lies in the testable domain, and that fraction is itself a lower bound on the exclusion, since the optically mapped inventory under-detects failures beneath canopy. The workflow is therefore an open-ground debris and topographic-change method that quantifies valley-floor and near-channel scour and deposition, not landslide source volumes under forest.

Roads are not inherently stable control in a landslide-affected landscape, where cut and fill slopes along roads were common initiation zones [9]. The PGCP median outvotes damaged or buried segments only while they remain a minority, as the A0069AR corridor shows, so candidate segments should be screened against mapped landslides and slope-modification records.

The change residual against the post-event LiDAR maps mainly the four months between the sortie and the LiDAR, together with residual SfM error (Figure 6). Split by LiDAR tile set, it averages +0.68 m (median −0.07 m) over the 6577 closure cells of the lower corridor and Lake Lure inflow, where sedimentation recorded by the SfM surface was cleared during cleanup, and −0.90 m (median −1.40 m) over the 10,447 cells of the reach through Chimney Rock village, where reconstruction placed fill that did not exist at the sortie; these two means, the −0.29 m closure mean of Section 3.2.3, and the +2.4 m over 187 m of road at Chimney Rock describe different footprints. Scheip et al. [8] report from repeat LiDAR across the same corridor that the geomorphic signatures of Helene obscure quickly as vegetation regrows and infrastructure is repaired. CAP-derived change standing above the post-event LiDAR change over the depositional lower corridor is that erasure seen from the opposite direction, although residual surface error cannot be excluded as a contributor.

Two temporal confounds bound the change maps themselves. First, the reference surface predates the storm by seven years, so any 2017–2024 change unrelated to Helene (bank migration, intervening high flows, and the construction and grading visible in the commercial strip) survives the LoD threshold. No change was excluded after the fact. Instead, a stratified random sample of the significant bare-earth change objects (40 valley and 39 gorge objects, Supplementary Note S14) was checked against the 2016–2019 and 2020–2023 NC OneMap orthoimagery, the CAP orthomosaic, and the post-Helene 2025 orthoimagery [38–40], labeling each object by the epoch in which disturbance inside it is first visible, with the sign and size of the change hidden [83], and volume shares were estimated for the stratified design [84–86]. Disturbance first visible in the October 2024 imagery, and absent in February 2023, holds 13% (95% CI 4–23%) of the valley gross volume and 46% (32–61%) of the gorge's. Earlier disturbance, mostly construction, grading, and quarrying, holds 42% (29–56%) and 10% (4–17%), and the rest shows no visible disturbance or cannot

be read, often where the interpreter judged the change a likely artifact. The volumes are therefore 2017-to-sortie change, of which a minority in the valley, and just under half in the gorge, dates to the sortie; the labels come from a single interpreter. Second, the sorties trail the storm by six to eight days, during which emergency access clearing, debris pushing, and road cutting were underway in both corridors and are identifiable in the 8 cm CAP orthomosaics, so some of the mapped scour and fill is machine work rather than flood work.

4.1. Refining CAP Aerial Photography for Volumetric Analysis

CAP flights are flown for orthomosaic production rather than 3D reconstruction, with GPS coordinates appended to the images after capture and neither real-time kinematic (RTK) positioning nor ground control [12,44]. Supplementary Table S15 contrasts them with unmanned aerial systems (UAS), which resolve small areas finely but need the ground access that storm damage removes [87]. The A0046B orthoimagery also contained patches of light and dark regions from variable camera ISO settings and Agisoft Metashape's mosaicking. The overexposed photos carried a high ISO setting (6400), which amplifies the sensor signal and raises image noise rather than admitting more light, and the underexposed photos combined ISO 200 with a 1/4000 s shutter (Table A1), whereas CAP aircrew guidance limits ISO to 400 or less [12]. The DSM shows no exposure-correlated artifacts on visual inspection, though a quantitative test was not performed. From the Metashape processing reports (Supplementary flight reports), the SfM chain took about 7.6 h of unattended time for A0046B on a laptop with an Intel Core i9-13900HX and an NVIDIA GeForce RTX 4070. That figure sums the matching, alignment, depth-map (2 h 7 min), dense-cloud, classification, DEM, and orthomosaic stages and excludes the mesh (2 h 57 min), which the analysis does not use. A0069AR, the smaller block (1443 against 1515 images), took about 22 h because its depth maps were generated on a workstation whose AMD Radeon RX 7600 needed 18 h 37 min for the stage that, by analogy with the A0046B run on the laptop's NVIDIA GPU, would take about 2 h; the difference is most plausibly hardware rather than a property of the flight. The downstream processing, from point-cloud export through GRASS surface construction (including the leave-one-out RST tuning), co-registration, bias modeling, and volumes, was not logged, and the archived chains ran between 19 and 23 March 2026 (A0046B) and 1 and 21 April 2026 (A0069AR) with gaps between stages, so an end-to-end turnaround was not demonstrated and none is claimed. Analyst interaction was not timed. The downstream GRASS chain runs unattended from one configuration file, but that file encodes the per-flight decisions of Section 2.3 with large consequences, the DTM interpolation method, the bias-model form, and the shift strategy, together with quality review.

Four conditions transfer the workflow beyond these corridors: (1) a paved state-road network of sufficient extent within the flight hull for PGCP control, (2) a pre-event QL1 or QL2 (USGS Quality Level 2) LiDAR reference, (3) a near-vertical archive flown at CAP's nominal 75/60 overlap setting, and (4) valley-confined relief that places open ground within reach of stable control. Only the dependence on relief and control geometry is quantified here (Sections 2.6 and 2.8); both flights used QL1 references and paved-road control, so the other conditions are requirements inferred from the workflow design rather than tested limits.

4.2. Spatially Variable DoD Accuracy Assessment for Volumetric Measurement

Per-cell uncertainty models are standard practice in DEM differencing [71,73,74,81,88], but an uncontrolled, opportunistic image source stresses them in ways a planned survey does not. The SfM residuals are heavy-tailed, so a Gaussian multiplier would understate the detection limit wherever the floor does not already carry the tail, a flexible bias field can

absorb its own noise estimate, and much of the footprint lies beyond the reach of any stable control, which is why the multiplier is calibrated on stable cells, the floor is cross-validated, and cells beyond control are reported as observed but untestable (Section 2.8). The 1.3 to 1.4 m co-registered bare-earth RMSE reported here sits five to seven times above the 0.20–0.25 m RMS of crewed-aircraft coastal SfM against LiDAR [15] and the sub-meter archival beach-dune DSMs of Almonacid-Caballer et al. [24], both from low-relief terrain with dense, well-distributed control. Here the vertical control runs only along valley-floor roads in high-relief valleys, and the error grows with height above it (Section 2.6), so the envelope is set by relief and control geometry rather than by the SfM reconstruction. The stable mask that calibrates these models is itself a choice. Above the valley floor its residual screen defines the fitting population, and rerunning the whole chain over screens of 3 to 10 m moves the gross terms by −4 to +11% in the valley and −20 to +15% in the gorge (Supplementary Note S12). That is small beside the spread between bias models but larger than the 5 to 7.5% systematic terms, so the volumes are stated conditional on the screen. The unthresholded budget (Supplementary Note S3) is not a better primary number here: integrated over millions of cells, systematic residuals of a few centimeters, such as the −0.03 m stable mean of the valley, exceed the propagated σ_V, so on both flights the thresholded tally is the defensible estimate.

5. Conclusions

This study supplies a stable-terrain accuracy assessment of the surfaces, and a consistency evaluation and false-positive bound for the change products, for a practice already used operationally during the Helene response, deriving volumetric topographic change from post-disaster CAP imagery [10,11]. The evidence comes from two flights over contrasting western North Carolina terrain and is not a general validation. The co-registered bare-earth surfaces reach 0.68 and 0.82 m NMAD against independent post-event LiDAR on stable terrain. In the Swannanoa Valley they resolve gross scour and fill of ~1.2–1.3 × 10^5 m^3 while the net is indistinguishable from zero, and the uncorrected difference reports five times the fill under the same limit. In the open-ground gorge corridor they record ~8 × 10^4 m^3 of positive change, about 7.3 × 10^4 m^3 of it deposition on land and the rest unattributed change on the 2017 Lake Lure surface. All volumes are lower bounds in coverage within the testable open-ground domain, with systematic terms of about 5% (valley, identified from check cells) and about 7.5% (gorge, a scale set by the intercept) of each gross term (deposition low, erosion high) and a false-positive component, bounded in Section 3.3 at 13 to 31% of a gross term if the flag rate measured inside the post-event LiDAR footprint holds across the testable domain, that runs against the coverage bound, measure 2017-to-sortie change, of which an image check dates about 13% of the valley gross volume and 46% of the gorge's to the sortie, and are conditional on the adopted bias model, the residual screen, and the fixed detection window, and the stable-ground diagnostics make the valley deposition term more likely an underestimate than an overestimate. Differences against the later LiDAR mix recovery work with residual SfM error rather than isolating either.

The method works for open-ground scour and deposition where intact paved roads supply vertical control, on valley floors, road corridors, and cleared parcels. It does not deliver building-scale change, where the DSM detection limit (10.6 m flight-wide average for A0046B) suppresses structure-edge artifacts and real structures alike. Nor does it deliver landslide debris volumes under closed canopy, where the bare-earth SfM surface does not reach the ground (NMAD 12.4 and 4.6 m under canopy taller than 10 m) and all but one of the 186 in-hull inventory landslides fall outside the testable domain. Extending the envelope onto the vegetated hillslopes where the damaging landslides initiated requires oblique imagery or fusion with a canopy-penetrating sensor. Within it, CAP imagery is a

rapid source for post-disaster debris and topographic-change assessment and can capture transient storage that later surveys cannot.

Supplementary Materials: The following supporting information can be downloaded at: https://www.mdpi.com/article/10.3390/rs18213766/s1. Supplementary Methods SM1: Data, datum handling, and Metashape parameters; SM2: Gaussian weighting for r.neighbors; Figure S1: Raw images from CAP flight A0046B; Figure S2: Local land-surface parameters for Flight A0046B; Figure S3: Uncorrected DTM DoD for Flight A0046B; Figure S4: Debiased DTM DoD for Flight A0046B; Figure S5: Local land-surface parameters for Flight A0069AR; Figure S6: The A0069AR analysis domain in the context of the full flight; Figure S7: Uncorrected bare-earth difference for Flight A0069AR; Figure S8: Debiased DTM DoD for Flight A0069AR; Figure S9: Workflow overview; Figure S10: GEOID12B minus GEOID18 separation over the two study areas; Figure S11: Registration and terrain-correlated bias, Flight A0046B bare earth; Figure S12: Agricultural field with raised overbank patches west of the commercial strip; Figure S13: Tributary reach west of the commercial strip; Figure S14: The Chimney Rock village reach of the Rocky Broad River corridor; Figure S15: Landslide above the Grovemont neighborhood of Swannanoa; Figure S16: Raw CAP frame over the Lake Lure inflow showing the floating debris raft; Figure S17: Local versus global first-return DSM LoD over the Swannanoa commercial strip; Table S1: Flight A0046B whole-scene DSM elevation statistics; Table S2: Bias-model sensitivity of the LoD-masked bare-earth volumes; Table S3: Local-LoD window sensitivity for Flight A0046B; Table S4: Local-LoD window sensitivity for Flight A0069AR; Table S5: Workflow-to-tool mapping; Table S6: Semivariogram parameters of the debiased stable-cell bare-earth residuals; Table S7: Stability of the Flight A0046B bare-earth volumes under a reallocation of the detection limit; Table S8: Estimates of the residual horizontal offset; Table S9: Residual-screen sensitivity of the bare-earth chain with the bias fit held fixed; Table S10: Screening recall for Flight A0046B; Table S11: Exclusion accounting for both flights; Table S12: Vertical accuracy of the SfM surfaces on sloped stable terrain; Table S13: Co-registration of the A0069AR SfM surfaces to the 2017 LiDAR; Table S14: Structure-from-motion block-strength diagnostics; Table S15: Operational trade-offs between UAS photogrammetry and CAP imagery; Table S16: Residual-screen sensitivity with the bias refitted and the local detection limit rebuilt; Table S17: Uncertainty of the road-median vertical shift; Table S18: Share of the significant bare-earth gross volume by the epoch in which disturbance is first visible; Note S1: Robustness checks; Note S2: Data and code; Note S3: Unthresholded, uncertainty-propagated budget; Note S4: Co-registration diagnostics and rejected alternatives; Note S5: Bias-correction diagnostics; Note S6: Level-of-Detection calibration and uncertainty details; Note S7: Geoid separation between the two LiDAR epochs; Note S8: Screening recall benchmark; Note S9: Exclusion accounting and landslide inventory overlay; Note S10: Site and diagnostic figures; Note S11: Additional tables; Note S12: Residual-screen sensitivity with the bias refitted; Note S13: Sampling and road-selection uncertainty of the road shift; Note S14: Image check of the change objects; Metashape processing reports for Flights A0046B and A0069AR. References [9,12,30,63–65,67,68,76,77,80,82–87,89–91] are cited in the Supplementary Materials.

Author Contributions: Conceptualization, W.R., C.T.W. and H.M.; methodology, C.T.W.; software, C.T.W.; validation, C.T.W. and P.R.; formal analysis, C.T.W. and P.R.; investigation, C.T.W.; resources, W.R., C.T.W., H.M.; data curation, C.T.W. and W.R.; writing—original draft preparation, C.T.W. and P.R.; writing—review and editing, C.T.W., W.R. and H.M.; visualization, C.T.W. and P.R.; supervision, C.T.W. and H.M.; project administration, C.T.W.; funding acquisition, H.M. All authors have read and agreed to the published version of the manuscript.

Funding: This research was funded by National Science Foundation (NSF) grant number 2303651 and the United States Department of Agriculture (USDA), Natural Resources Conservation Service (NRCS) Cooperative Agreement NR233A750023C043.

Institutional Review Board Statement: Not applicable.

Informed Consent Statement: Not applicable.

Data Availability Statement: The source data are openly available in the public domain: Civil Air Patrol imagery through the CAP incident-imagery archive [30], NC statewide LiDAR and or-

thoimagery, including the 2020–2023 and post-Helene 2025 orthoimagery services, through NC OneMap and the USGS 3D Elevation Program [34–36,38–40], and road and parcel vectors through NCDOT and NC OneMap [41,43]. The GRASS processing tools are released as the open-source r.dem toolset in the OSGeo grass-addons repository, documented at https://grass.osgeo.org/grass-devel/manuals/addons/r.dem.html (accessed on 25 October 2026), with an archived snapshot on Zenodo at https://doi.org/10.5281/zenodo.21940875. The classified SfM point clouds, the digital surface and terrain models before the vertical shift (EXIF mean-sea-level heights with no realized vertical datum), and the orthomosaics are available from the OpenTopography Community Dataspace. The surfaces shifted to NAVD88 heights, the DEM-of-difference and level-of-detection rasters, the Metashape batch scripts and run logs, the two per-flight configuration files, which record every applied parameter except those of the interactive classification, which were not logged (Section 2.3), and the processing code (version 1.0.0) are archived on Zenodo at https://doi.org/10.5281/zenodo.23790929, which also lists the OpenTopography dataset DOIs. The classified A0069AR point cloud is that flight's reproducibility entry point, from which every downstream step can be rerun.

Acknowledgments: We acknowledge the residents of western North Carolina and emergency personnel who provided ground knowledge and pointed us to data resources. We also acknowledge the U.S. Army Engineer Research and Development Center (ERDC), which coordinated the response to generate DSMs to aid in the relief effort, and the students of the North Carolina State University UAS Mapping and Analysis Course (GIS 584) in the fall of 2024 who chose to help in the relief process by processing CAP imagery for their final projects. During the preparation of this manuscript, the authors used Claude (Anthropic; Fable and Opus models, 2026) to assist with editing text, formatting the manuscript, and developing analysis and figure-generation code. All methods, results, and interpretations were developed, verified, and approved by the authors, who take full responsibility for the content of this publication.

Conflicts of Interest: The author William Reckling notes that the views expressed by him in this article are solely his own and do not necessarily represent the views of the Geospatial Research Laboratory (GRL), the Engineer Research and Development Center (ERDC), the U.S. Army Corps of Engineers (USACE), the Department of the Army, the Department of War (DoW), or the United States Government. Author Corey T. White was employed by the company OpenPlains Inc. The remaining authors declare that the research was conducted in the absence of any commercial or financial relationships that could be construed as a potential conflict of interest.

Abbreviations

The following abbreviations are used in this manuscript:

CAP	Civil Air Patrol
LiDAR	Light detection and ranging
NDVI	Normalized Difference Vegetation Index
NHD	National Hydrography Dataset
OPR	Original product resolution
DEM	Digital elevation model
DSM	Digital surface model
DTM	Digital terrain model
UAS	Unmanned aerial system
SfM	Structure-from-motion
GCP	Ground control point
GSD	Ground sampling distance
PGCP	Pseudo ground control point
RMSE	Root mean square error
NMAD	Normalized median absolute deviation
DoD	DEM of difference
LoD	Level of Detection
NVA	Non-vegetated vertical accuracy
VVA	Vegetated vertical accuracy

CoCoRaHS	Community Collaborative Rain, Hail and Snow Network
GNIS	Geographic Names Information System
ICP	Iterative closest point
ME	Mean error
MED	Median error
NHC	National Hurricane Center
NID	National Inventory of Dams
NWIS	National Water Information System
QL1	USGS Quality Level 1
RST	Regularized spline with tension
RTK	Real-time kinematic
TIGER	Topologically Integrated Geographic Encoding and Referencing

Appendix A

Table A1. Summary statistics of Flight A0046B nadir photo characteristics.

Stat	ISO	Shutter	Aperture	Brightness	MSL Alt (m) *
mean	1296	1/2000	f/5.6	96.5	1706
min	200	1/4000	f/5.6	6.2	1637
25%	640	1/2000	f/5.6	73.1	1670
50%	1000	1/2000	f/5.6	93.2	1726
75%	1600	1/2000	f/5.6	112.1	1734
max	6400	1/2000	f/5.6	246.3	1754
std	1032	–	–	36.1	36

* MSL Alt is the EXIF GPS altitude above mean sea level as referenced by the receiver's geoid model, not a NAVD88 height. Brightness is the per-image mean 8-bit luminance (0 to 255) computed from the frames. Aperture was fixed at f/5.6; shutter statistics are the distribution of exposure times.

References

1. Cohen, M.C.L.; de Souza, A.V.; Liu, K.B.; Yao, Q. A timely method for post-disaster assessment and coastal landscape survey using drone and satellite imagery. *MethodsX* **2023**, *10*, 102065. [CrossRef] [PubMed]
2. Wang, Q.; Li, W.; Yu, Z.; Abbasi, Q.; Imran, M.; Ansari, S.; Sambo, Y.; Wu, L.; Li, Q.; Zhu, T. An Overview of Emergency Communication Networks. *Remote Sens*. **2023**, *15*, 1595. [CrossRef]
3. Khan, A.; Gupta, S.; Gupta, S.K. Multi-hazard disaster studies: Monitoring, detection, recovery, and management, based on emerging technologies and optimal techniques. *Int. J. Disaster Risk Reduct*. **2020**, *47*, 101642. [CrossRef]
4. Karaer, A.; Chen, M.; Gazzea, M.; Ghorbanzadeh, M.; Abichou, T.; Arghandeh, R.; Ozguven, E.E. Remote sensing-based comparative damage assessment of historical storms and hurricanes in Northwestern Florida. *Int. J. Disaster Risk Reduct*. **2022**, *72*, 102857. [CrossRef]
5. Ansari, R.A.; Esimaje, T.; Ibrahim, O.M.; Mulrooney, T. Analysis of Forest Change Detection Induced by Hurricane Helene Using Remote Sensing Data. *Forests* **2025**, *16*, 788. [CrossRef]
6. Lu, P.; Ding, H.; Tian, X. DFANet: A Deep Feature Attention Network for Building Change Detection in Remote Sensing Imagery. *Remote Sens*. **2025**, *17*, 2575. [CrossRef]
7. Kumari, S.; Agarwal, S.; Agrawal, N.K.; Agarwal, A.; Garg, M.C. A Comprehensive Review of Remote Sensing Technologies for Improved Geological Disaster Management. *Geol. J*. **2025**, *60*, 223–235. [CrossRef]
8. Scheip, C.; Lang, K.; Prince, P.; Wegmann, K.; Wooten, R.; Reynolds, A.; Harris, D.A. A storm-sculpted landscape: Observations from post-Helene lidar in the Hickory Nut Gorge, North Carolina. *Earth Surf. Processes Landf*. **2026**, *51*, e70228. [CrossRef]
9. Schaefer, L.N.; Rengers, F.K.; Mirus, B.B.; Toney, L.; Allstadt, K.E.; Wooten, R.M.; Moore, P.; Burgi, P.M.; Witt, A.; Bilderback, E.L.; et al. Insights into Widespread Landsliding in Southern Appalachia from Hurricane Helene. *GSA Today* **2026**, *36*, 4–11. [CrossRef]
10. Coleman, C.C. ERDC Researchers Use 2D, 3D Modeling to Aid in Hurricane Debris Assessment. U.S. Army Engineer Research and Development Center, News Stories. 2024. Available online: https://www.erdc.usace.army.mil/Media/News-Stories/Article/3960701/erdc-researchers-use-2d-3d-modeling-to-aid-in-hurricane-debris-assessment/ (accessed on 11 August 2026).

11. White, C. Topographic Impacts of Hurricane Helene in Western North Carolina. Presented at the IALE-North America Annual Meeting, Raleigh, NC, USA, 13–17 April 2025. Available online: https://zenodo.org/records/15237651 (accessed on 25 October 2026). [CrossRef]
12. Civil Air Patrol U.S. Air Force Auxiliary. Airborne Photographer. 2024. Available online: https://nesa.cap.gov/media/cms/MART_Volume_III__June_2024_007AD7E360F08.pdf (accessed on 14 October 2026).
13. NOAA National Ocean Service. Emergency Response Imagery. 2025. Available online: https://oceanservice.noaa.gov/hazards/emergency-response-imagery.html (accessed on 11 August 2026).
14. NOAA National Geodetic Survey. NGS Emergency Response Imagery Online Viewer. Hurricane Helene Collection, 27 September to 8 October 2024; Western North Carolina 5 to 8 October 2024. Available online: https://storms.ngs.noaa.gov/ (accessed on 11 August 2026).
15. Sherwood, C.R.; Warrick, J.A.; Hill, A.D.; Ritchie, A.C.; Andrews, B.D.; Plant, N.G. Rapid, Remote Assessment of Hurricane Matthew Impacts Using Four-Dimensional Structure-from-Motion Photogrammetry. *J. Coast. Res.* **2018**, *34*, 1303–1316. [CrossRef]
16. Aggarwal, D.; Gautam, S.; Whitehurst, D.; Kochersberger, K. Post-Hurricane Debris and Community Flood Damage Assessment Using Aerial Imagery. *Remote Sens.* **2025**, *17*, 3171. [CrossRef]
17. Voigt, S.; Giulio-Tonolo, F.; Lyons, J.; Kučera, J.; Jones, B.; Schneiderhan, T.; Platzeck, G.; Kaku, K.; Hazarika, M.K.; Czaran, L.; et al. Global trends in satellite-based emergency mapping. *Science* **2016**, *353*, 247–252. [CrossRef] [PubMed]
18. Shean, D.E.; Alexandrov, O.; Moratto, Z.M.; Smith, B.E.; Joughin, I.R.; Porter, C.; Morin, P. An automated, open-source pipeline for mass production of digital elevation models (DEMs) from very-high-resolution commercial stereo satellite imagery. *ISPRS J. Photogramm. Remote Sens.* **2016**, *116*, 101–117. [CrossRef]
19. Berthier, E.; Vincent, C.; Magnússon, E.; Gunnlaugsson, Á.Þ.; Pitte, P.; Le Meur, E.; Masiokas, M.; Ruiz, L.; Pálsson, F.; Belart, J.M.C.; et al. Glacier topography and elevation changes derived from Pléiades sub-meter stereo images. *Cryosphere* **2014**, *8*, 2275–2291. [CrossRef]
20. Bhushan, S.; Shean, D.; Alexandrov, O.; Henderson, S. Automated digital elevation model (DEM) generation from very-high-resolution Planet SkySat triplet stereo and video imagery. *ISPRS J. Photogramm. Remote Sens.* **2021**, *173*, 151–165. [CrossRef]
21. Knuth, F.; Shean, D.; Bhushan, S.; Schwat, E.; Alexandrov, O.; McNeil, C.; Dehecq, A.; Florentine, C.; O'Neel, S. Historical Structure from Motion (HSfM): Automated processing of historical aerial photographs for long-term topographic change analysis. *Remote Sens. Environ.* **2023**, *285*, 113379. [CrossRef]
22. Bakker, M.; Lane, S.N. Archival photogrammetric analysis of river–floodplain systems using Structure from Motion (SfM) methods. *Earth Surf. Processes Landf.* **2017**, *42*, 1274–1286. [CrossRef]
23. Chirico, P.; DeWitt, J.; Bergstresser, S. Evaluating Elevation Change Thresholds between Structure-from-Motion DEMs Derived from Historical Aerial Photos and 3DEP LiDAR Data. *Remote Sens.* **2020**, *12*, 1625. [CrossRef]
24. Almonacid-Caballer, J.; Cabezas-Rabadán, C.; Gorkovchuk, D.; Palomar-Vázquez, J.; Pardo-Pascual, J.E. Re-Using Historical Aerial Imagery for Obtaining 3D Data of Beach-Dune Systems: A Novel Refinement Method for Producing Precise and Comparable DSMs. *Remote Sens.* **2025**, *17*, 594. [CrossRef]
25. Voglino, B.; Godone, D.; Baldo, M.; Bono, B.; Luino, F.; Bonomelli, R.; Colosio, P.; Beretta, L.; Albertelli, L.; Turconi, L. Application of Structure from Motion Techniques Using Historical Aerial Images, Orthomosaics, and Aerial LiDAR Point Cloud Datasets for the Investigation of Debris Flow Source Areas. *Remote Sens.* **2025**, *17*, 3658. [CrossRef]
26. White, C.T. r.dem: GRASS Addon Toolset for DEM Co-Registration, Differencing, and Topographic Change Analysis, 2026. Software Archived on Zenodo; Released in OSGeo Grass-Addons. Available online: https://zenodo.org/records/21940875 (accessed on 25 October 2026). [CrossRef]
27. GRASS Development Team; Landa, M.; Neteler, M.; Metz, M.; Petrasova, A.; Petras, V.; Clements, G.; Zigo, T.; Larsson, N.; Kladivova, L.; et al. *GRASS*, Version 8.5.0; Zenodo: Geneva, Switzerland, 2026. [CrossRef]
28. Hagen, A.B.; Cangialosi, J.P.; Chenard, M.; Alaka, L.; Delgado, S. Hurricane Helene. Tropical Cyclone Report AL092024, NOAA National Hurricane Center. 2025. Available online: https://www.nhc.noaa.gov/data/tcr/AL092024_Helene.pdf (accessed on 14 October 2026).
29. U.S. Geological Survey. Peak Streamflow for the Nation: USGS 03451000 Swannanoa River at Biltmore, NC. National Water Information System. 2026. Available online: https://nwis.waterdata.usgs.gov/nwis/peak?site_no=03451000 (accessed on 14 October 2026).
30. Civil Air Patrol U.S. Air Force Auxiliary. Civil Air Patrol—Helene NADIR & Oblique Aerial Photos. 2024. Available online: https://services.arcgis.com/XG15cJAlne2vxtgt/ArcGIS/rest/services/Image_Points_view/FeatureServer (accessed on 14 October 2026).
31. Town of Lake Lure. Hurricane Helene Summary Memo. 2024. Available online: https://www.townoflakelure.com/dam/page/hurricane-helene-summary-memo (accessed on 3 March 2026).

32. U.S. Army Corps of Engineers. USACE and Town of Lake Lure Mark Completion of Hurricane Helene Recovery Work. 2025. Available online: https://www.dvidshub.net/news/551888/usace-and-town-lake-lure-mark-completion-hurricane-helene-recovery-work (accessed on 30 July 2026).
33. NOAA National Hurricane Center. Best-Track File AL092024 (Helene), Automated Tropical Cyclone Forecast Archive. 2025. Available online: https://ftp.nhc.noaa.gov/atcf/archive/2024/bal092024.dat.gz (accessed on 14 October 2026).
34. U.S. Geological Survey. USGS Original Product Resolution (OPR) Digital Elevation Model NC_Phase5_2018_A18, Work Units NC_Phase5_Buncombe_2017 and NC_Phase5_Rutherford_2017. 2022. Available online: https://rockyweb.usgs.gov/vdelivery/Datasets/Staged/Elevation/OPR/Projects/NC_Phase5_2018_A18/ (accessed on 14 October 2026).
35. NC Emergency Management GIS Section. North Carolina Spatial Data Download. 2024. Available online: https://sdd.nc.gov/ (accessed on 21 October 2024).
36. U.S. Geological Survey. USGS Lidar Point Cloud NC_Phase5_2018_A18. Buncombe and Rutherford County Work Units of the Same Project. 2021. Available online: https://rockyweb.usgs.gov/vdelivery/Datasets/Staged/Elevation/LPC/Projects/NC_Phase5_2018_A18/NC_Phase5_Buncombe_2017/ (accessed on 8 April 2025).
37. North Carolina Emergency Management; NC Collaboratory. North Carolina Post-Hurricane Helene LiDAR (January to February 2025). North Carolina Spatial Data Download. Post-Event LiDAR Acquisition. 2025. Available online: https://sdd.nc.gov/ (accessed on 11 August 2026).
38. NC OneMap/State of North Carolina. Statewide Ortho Tile Index, 2012 and Later (Source of the 2019 Orthoimagery Tiles). 2025. Available online: https://data-nconemap.opendata.arcgis.com/datasets/statewide-ortho-tile-index-2012-and-later (accessed on 7 August 2025).
39. NC OneMap/State of North Carolina. NC Statewide Orthoimagery 2020–2023 (Image Service). Pre-Event Chips for the Change-Residual Site Figure. 2023. Available online: https://services.nconemap.gov/secure/rest/services/Imagery/Orthoimagery_2020_2023/ImageServer (accessed on 11 August 2026).
40. NC OneMap/State of North Carolina. NC Post-Hurricane Helene Orthoimagery 2025 (Image Service). Post-Event Chips for the Change-Residual Site Figure. 2025. Available online: https://services.nconemap.gov/secure/rest/services/Imagery/Orthoimagery_Helene_2025/ImageServer (accessed on 11 August 2026).
41. North Carolina Department of Transportation. NC OneMap State Maintained Roads. Quarterly Service; the 2026 Q1 Snapshot was Imported on 25 March 2026. 2026. Available online: https://www.nconemap.gov/datasets/NCDOT::state-maintained-roads/about (accessed on 25 March 2026).
42. U.S. Geological Survey. National Hydrography Dataset (NHD): Flowline Layer of the NHD Map Service. Layer 6, Clipped to Each Flight Hull. 2026. Available online: https://hydro.nationalmap.gov/arcgis/rest/services/nhd/MapServer (accessed on 2 July 2026).
43. NC OneMap/State of North Carolina. North Carolina Parcels (Polygons). 2025. Available online: https://www.nconemap.gov/datasets/nconemap::north-carolina-parcels-polygons (accessed on 7 August 2025).
44. Civil Air Patrol U.S. Air Force Auxiliary. Ortho—Draft Revision Sep 24. In *Mission Aircrew Reference Text*; Civil Air Patrol National Headquarters: Maxwell Air Force Base, AL, USA, 2024; Volume IV. Draft Volume. Available online: https://nesa.cap.gov/media/cms/CAP_Ortho_MART_Vol_4_Draft_V1_FF2D2B3620289.pdf (accessed on 14 October 2026).
45. Morgan, H. 2017 Digital Elevation Model at a 3.125 foot Resolution for Phase Five Counties in North Carolina. In *FGDC Metadata Record, 1 August 2018*; North Carolina Emergency Management: Raleigh, NC, USA, 2018.
46. ESP Associates, Inc. *North Carolina Floodplain Mapping Program: Phase 5 LiDAR Post-Processing Report, Delivery Order 35*; Technical Report 286-000030 ESP; Prepared for North Carolina Emergency Management; ESP Associates, Inc.: Fort Mill, SC, USA, 2019.
47. North Carolina Geographic Information Coordinating Council. Minutes, Statewide Mapping Advisory Committee Meeting, 10 April 2025. Available online: https://it.nc.gov/smac-minutes-april-10-2025/open (accessed on 14 October 2026).
48. U.S. Geological Survey. Lidar Base Specification, Version 2.1. National Geospatial Program Standards and Specifications. 2019. Available online: https://www.usgs.gov/3DEP/lidarspec (accessed on 14 October 2026).
49. NOAA National Geodetic Survey. GEOID12B Hybrid Geoid Model. Grid us_noaa_g2012bu0.tif as Distributed by PROJ-Data. 2015. Available online: https://geodesy.noaa.gov/GEOID/GEOID12B/ (accessed on 11 August 2026).
50. Ahlgren, K.; Scott, G.; Zilkoski, D.; Shaw, B.; Paudel, N. GEOID18. NOAA Technical Report NOS NGS 72; NOAA National Geodetic Survey: Silver Spring, MD, USA, 2020.
51. Open Source Geospatial Foundation. PROJ-data: Grids for Coordinate Transformations. 2024. Available online: https://github.com/OSGeo/PROJ-data (accessed on 11 August 2026).
52. Agisoft LLC. *Agisoft Metashape Professional*, Version 2.2; Software for Photogrammetric Processing of Digital Images and 3D Spatial Data Generation; Agisoft LLC: St. Petersburg, Russia, 2024.
53. Westoby, M.J.; Brasington, J.; Glasser, N.F.; Hambrey, M.J.; Reynolds, J.M. 'Structure-from-Motion' photogrammetry: A low-cost, effective tool for geoscience applications. *Geomorphology* **2012**, *179*, 300–314. [CrossRef]

54. Fonstad, M.A.; Dietrich, J.T.; Courville, B.C.; Jensen, J.L.; Carbonneau, P.E. Topographic structure from motion: A new development in photogrammetric measurement. *Earth Surf. Processes Landf.* **2013**, *38*, 421–430. [CrossRef]
55. Grybas, H.; Congalton, R.G. A Comparison of Multi-Temporal RGB and Multispectral UAS Imagery for Tree Species Classification in Heterogeneous New Hampshire Forests. *Remote Sens.* **2021**, *13*, 2631. [CrossRef]
56. Barbasiewicz, A.; Widerski, T.; Daliga, K. The analysis of the accuracy of spatial models using photogrammetric software: Agisoft Photoscan and Pix4D. *Proc. E3S Web Conf.* **2018**, *26*, 00012. [CrossRef]
57. Jasińska, A.; Pyka, K.; Pastucha, E.; Midtiby, H.S. A Simple Way to Reduce 3D Model Deformation in Smartphone Photogrammetry. *Sensors* **2023**, *23*, 728. [CrossRef] [PubMed]
58. Śledź, S.; Ewertowski, M.W. Evaluation of the Influence of Processing Parameters in Structure-from-Motion Software on the Quality of Digital Elevation Models and Orthomosaics in the Context of Studies on Earth Surface Dynamics. *Remote Sens.* **2022**, *14*, 1312. [CrossRef]
59. Swayze, N.C.; Tinkham, W.T.; Vogeler, J.C.; Hudak, A.T. Influence of flight parameters on UAS-based monitoring of tree height, diameter, and density. *Remote Sens. Environ.* **2021**, *263*, 112540. [CrossRef]
60. Mitášová, H.; Mitáš, L. Interpolation by regularized spline with tension: I. Theory and implementation. *Math. Geol.* **1993**, *25*, 641–655. [CrossRef]
61. Mitášová, H.; Hofierka, J. Interpolation by regularized spline with tension: II. Application to terrain modeling and surface geometry analysis. *Math. Geol.* **1993**, *25*, 657–669. [CrossRef]
62. Mitasova, H.; Mitas, L.; Harmon, R. Simultaneous Spline Approximation and Topographic Analysis for Lidar Elevation Data in Open-Source GIS. *IEEE Geosci. Remote Sens. Lett.* **2005**, *2*, 375–379. [CrossRef]
63. Cressie, N.; Hawkins, D.M. Robust Estimation of the Variogram: I. *J. Int. Assoc. Math. Geol.* **1980**, *12*, 115–125. [CrossRef]
64. Künsch, H.R. The Jackknife and the Bootstrap for General Stationary Observations. *Ann. Stat.* **1989**, *17*, 1217–1241. [CrossRef]
65. Davison, A.C.; Hinkley, D.V. *Bootstrap Methods and Their Application*; Cambridge University Press: Cambridge, UK, 1997. [CrossRef]
66. Nuth, C.; Kääb, A. Co-registration and bias corrections of satellite elevation data sets for quantifying glacier thickness change. *Cryosphere* **2011**, *5*, 271–290. [CrossRef]
67. Wang, Y.; Li, J.; Duan, P.; Wang, R.; Yu, X. The DEM Registration Method Without Ground Control Points for Landslide Deformation Monitoring. *Remote Sens.* **2024**, *16*, 4236. [CrossRef]
68. Guizar-Sicairos, M.; Thurman, S.T.; Fienup, J.R. Efficient subpixel image registration algorithms. *Opt. Lett.* **2008**, *33*, 156–158. [CrossRef] [PubMed]
69. James, M.R.; Robson, S. Mitigating systematic error in topographic models derived from UAV and ground-based image networks. *Earth Surf. Processes Landf.* **2014**, *39*, 1413–1420. [CrossRef]
70. Brasington, J.; Langham, J.; Rumsby, B. Methodological sensitivity of morphometric estimates of coarse fluvial sediment transport. *Geomorphology* **2003**, *53*, 299–316. [CrossRef]
71. Wheaton, J.M.; Brasington, J.; Darby, S.E.; Sear, D.A. Accounting for uncertainty in DEMs from repeat topographic surveys: improved sediment budgets. *Earth Surf. Processes Landf.* **2010**, *35*, 136–156. [CrossRef]
72. Mitasova, H.; Overton, M.F.; Recalde, J.J.; Bernstein, D.J.; Freeman, C.W. Raster-Based Analysis of Coastal Terrain Dynamics from Multitemporal Lidar Data. *J. Coast. Res.* **2009**, *25*, 507–514. [CrossRef]
73. Bailey, G.; Li, Y.; McKinney, N.; Yoder, D.; Wright, W.; Washington-Allen, R. Las2DoD: Change Detection Based on Digital Elevation Models Derived from Dense Point Clouds with Spatially Varied Uncertainty. *Remote Sens.* **2022**, *14*, 1537. [CrossRef]
74. He, Y.; Lei, S.; Dai, W.; Chen, X.; Wang, B.; Sheng, Y.; Lin, H. DEM-based topographic change detection considering the spatial distribution of errors. *Geo-Spat. Inf. Sci.* **2025**, *28*, 497–510. [CrossRef]
75. Höhle, J.; Höhle, M. Accuracy assessment of digital elevation models by means of robust statistical methods. *ISPRS J. Photogramm. Remote Sens.* **2009**, *64*, 398–406. [CrossRef]
76. James, M.R.; Robson, S.; Smith, M.W. 3-D uncertainty-based topographic change detection with structure-from-motion photogrammetry: Precision maps for ground control and directly georeferenced surveys. *Earth Surf. Processes Landf.* **2017**, *42*, 1769–1788. [CrossRef]
77. Anderson, S.W. Uncertainty in quantitative analyses of topographic change: Error propagation and the role of thresholding. *Earth Surf. Processes Landf.* **2019**, *44*, 1015–1033. [CrossRef]
78. Hugonnet, R.; Brun, F.; Berthier, E.; Dehecq, A.; Mannerfelt, E.S.; Eckert, N.; Farinotti, D. Uncertainty Analysis of Digital Elevation Models by Spatial Inference From Stable Terrain. *IEEE J. Sel. Top. Appl. Earth Obs. Remote Sens.* **2022**, *15*, 6456–6472. [CrossRef]
79. Milan, D.J.; Heritage, G.L.; Large, A.R.G.; Fuller, I.C. Filtering spatial error from DEMs: Implications for morphological change estimation. *Geomorphology* **2011**, *125*, 160–171. [CrossRef]
80. Rolstad, C.; Haug, T.; Denby, B. Spatially integrated geodetic glacier mass balance and its uncertainty based on geostatistical analysis: Application to the western Svartisen ice cap, Norway. *J. Glaciol.* **2009**, *55*, 666–680. [CrossRef]
81. Lane, S.N.; Westaway, R.M.; Murray Hicks, D. Estimation of erosion and deposition volumes in a large, gravel-bed, braided river using synoptic remote sensing. *Earth Surf. Processes Landf.* **2003**, *28*, 249–271. [CrossRef]

82. Burgi, P.M.; Toney, L.D.; Collins, E.A.; Murphy, C.R.; Ellison, S.M.; Schmitt, R.G.; Allstadt, K.E.; Bedinger, E.C.; Belair, G.M.; Bilderback, E.L.; et al. Preliminary Landslide Inventory for Landslides Triggered by Hurricane Helene (September 2024); U.S. Geological Survey Data Release; U.S. Geological Survey: Reston, VA, USA, 2025. [CrossRef]
83. Cohen, W.B.; Yang, Z.; Kennedy, R. Detecting Trends in Forest Disturbance and Recovery Using Yearly Landsat Time Series: 2. TimeSync, Tools for Calibration and Validation. *Remote Sens. Environ.* **2010**, *114*, 2911–2924. [CrossRef]
84. Cochran, W.G. *Sampling Techniques*, 3rd ed.; John Wiley & Sons: New York, NY, USA, 1977.
85. Stehman, S.V. Estimating Area and Map Accuracy for Stratified Random Sampling When the Strata Are Different from the Map Classes. *Int. J. Remote Sens.* **2014**, *35*, 4923–4939. [CrossRef]
86. Olofsson, P.; Foody, G.M.; Herold, M.; Stehman, S.V.; Woodcock, C.E.; Wulder, M.A. Good Practices for Estimating Area and Assessing Accuracy of Land Change. *Remote Sens. Environ.* **2014**, *148*, 42–57. [CrossRef]
87. White, C.T.; Reckling, W.; Petrasova, A.; Meentemeyer, R.K.; Mitasova, H. Rapid-DEM: Rapid Topographic Updates through Satellite Change Detection and UAS Data Fusion. *Remote Sens.* **2022**, *14*, 1718. [CrossRef]
88. Capolupo, A. Improving the Accuracy of Global DEM of Differences (DoD) in Google Earth Engine for 3-D Change Detection Analysis. *IEEE J. Sel. Top. Appl. Earth Obs. Remote Sens.* **2021**, *14*, 12332–12347. [CrossRef]
89. Armenakis, C.; Gao, Y.; Sohn, G. Semi-Automatic Co-Registration of Photogrammetric and LiDAR Data Using Buildings. *ISPRS Ann. Photogramm. Remote Sens. Spat. Inf. Sci.* **2012**, *I-3*, 13–18. [CrossRef]
90. Heid, T.; Kääb, A. Evaluation of existing image matching methods for deriving glacier surface displacements globally from optical satellite imagery. *Remote Sens. Environ.* **2012**, *118*, 339–355. [CrossRef]
91. Yoshida, K.; Endo, R.; Iwahashi, J.; Sasagawa, A.; Yarai, H. Aerial SfM–MVS Visualization of Surface Deformation along Folds during the 2024 Noto Peninsula Earthquake (Mw7.5). *Remote Sensing* **2024**, *16*, 2813. [CrossRef]

Disclaimer/Publisher's Note: The statements, opinions and data contained in all publications are solely those of the individual author(s) and contributor(s) and not of MDPI and/or the editor(s). MDPI and/or the editor(s) disclaim responsibility for any injury to people or property resulting from any ideas, methods, instructions or products referred to in the content.